Sustained ErbB activation causes demyelination and hypomyelination by driving necroptosis of mature oligodendrocytes and apoptosis of oligodendrocyte precursor cells

Authors

Xu Hu,[1,†] Guanxiu Xiao,[1,†] Li He,[1,†] Xiaojie Niu,[1] Huashun Li,[1] Qi Xu,[1] Zhengdong Wei,[1] Mengsheng Qiu,[1] Kenji F. Tanaka,[2] Ying Shen,[3] and Yanmei Tao[1,*]

Affiliations

[1]Key Lab of Organ Development and Regeneration of Zhejiang Province, Institute of Life Sciences, College of Life and Environmental Sciences, Hangzhou Normal University, Hangzhou 310000, China.

[2]Department of Neuropsychiatry, Keio University School of Medicine, Tokyo 160-8582, Japan.

[3]Department of Neurobiology, Key Laboratory of Medical Neurobiology of Zhejiang Province, Zhejiang University School of Medicine, Hangzhou 310058, China.

[†]These authors contributed equally.

Corresponding Author: [*]Correspondence and requests for materials should be addressed to Y.T. (e-mail: ytao@hznu.edu.cn)

Abstract

Oligodendrocytes are vulnerable to genetic and environmental insults and its injury leads to demyelinating diseases. The roles of ErbB receptors in the CNS myelin integrity are largely unknown. Here we overactivate ErbB receptors that mediate signaling of either neuregulin or EGF family growth factors and found their synergistic activation caused deleterious outcomes in white matter. Sustained ErbB activation induced by the tetracycline-dependent mouse tool *Plp*-tTA resulted in demyelination, axonal degeneration, oligodendrocyte precursor cell (OPC) proliferation, astrogliosis, and microgliosis in white matter. Moreover, there was hypermyelination prior to these pathological events. In contrast, sustained ErbB activation induced by another tetracycline-dependent mouse tool *Sox10*$^{+/rtTA}$ caused hypomyelination in the corpus callosum and optic nerve, which appeared to be a developmental deficit and did not associate with OPC regeneration, astrogliosis, or microgliosis. By analyzing the differentiation states of cells that were pulse-labeled with a viral reporter, we found that, during juvenile to adolescent development, *Plp*-tTA targeted mainly mature oligodendrocytes (MOs), while *Sox10*$^{+/rtTA}$ targeted OPCs and newly-formed oligodendrocytes. The distinct phenotypes of mice with ErbB overactivation induced by *Plp*-tTA and *Sox10*$^{+/rtTA}$ supported the reporter pulse-labeling results, and consolidated their non-overlapping targeting preferences in the oligodendrocyte lineage after early development. These features enabled us to demonstrate that ErbB overactivation in MOs induced necroptosis that caused pathological demyelination, whereas in OPCs induced apoptosis that caused developmental hypomyelination. These results established an upstream pathogenic role of ErbB

overactivation in oligodendrocytes, providing molecular and cellular insights into the primary oligodendropathy in demyelinating diseases.

Keywords: ErbB signaling, necroptosis, apoptosis, oligodendropathy, demyelinating disease

Introduction

Oligodendrocytes form myelin to speed up the axonal impulse conduction while supporting neuronal function and integrity in the central nervous system (CNS). White matter is expanded, with a growth peak during juvenile to adolescence, by oligodendrocyte precursor cells (OPCs) that proliferate and differentiate into newly-formed oligodendrocytes (NFOs) under stringent regulation by extrinsic and intrinsic signals (1, 2). NFOs progress from pre-myelinating oligodendrocytes to newly myelinating oligodendrocytes. Myelinating oligodendrocytes effectively generate myelin sheaths in a short time window before further differentiating into mature oligodendrocytes (MOs) that are extremely stable in maintaining myelin sheaths (3-7). Oligodendrocyte injury can be induced by genetic factors, autoimmune responses, or microenvironmental insults from ischemia, trauma, viruses, or toxins, leading to demyelinating diseases (8). Understanding the pathogenetic mechanisms is essential for developing strategies to combat myelin loss and promote myelin restoration.

Intracellular signaling pathways, such as MAPK, Akt, and mTOR, are activated to promote oligodendrocyte differentiation, survival, and myelination (9-12). Tyrosine kinase receptors ErbB(1-4), mediating abovementioned signal transduction pathways, are known to be fundamental to various neural developmental events (13). Numerous growth factors are able to activate ErbB receptors, including the neuregulin (NRG) family (NRG1-NRG6) and the epidermal growth factor (EGF) family (EGF, HB-EGF, TGFα, amphiregulin, epiregulin, β-cellulin, and epigen). Among them, most of the EGF family ligands bind to EGFR only, and the NRG family ligands bind to ErbB3 and ErbB4, except that HB-EGF, β-cellulin, and epiregulin can bind both EGFR and ErbB4 (13). Ligand binding stimulates

ErbB receptors dimerize with one another or preferentially with ErbB2 to activate multiple downstream signaling pathways (13).

Although it is well-established that ErbB2 and ErbB3 that mediate NRG signaling are crucial to Schwann cell survival and maturation in the peripheral nervous system (14), the roles of ErbB receptors in oligodendrocytes have long been debated. For example, ErbB3 has been reported to be dispensable for oligodendrocyte development (15), and ErbB3/ErbB4 double knockout from embryonic age does not result in CNS myelin alteration (16). However, there are other reports that indicate inducing ErbB3 depletion in oligodendrocytes by *Plp*-CreER from postnatal day 19 (P19) results in adult hypomyelination (17, 18). Studies on oligodendrocyte-specific knock-out mice have validated the expression of ErbB3 and ErbB4 in oligodendrocytes (16), while phosphorylated EGFR is detected in oligodendrocytes by immunostaining (19). Despites the controversial results from loss-of-function studies, overexpressing NRG1 Type I or Type III in neurons, or hEGFR in oligodendrocytes (*CNP*-hEGFR), promotes the CNS myelination (16, 20). Interestingly, transgenic mice *CNP*-hEGFR increases the numbers of myelinated axons but not myelin thickness (20), whereas NRG1-overexpressing mice reveal hypermyelination in white matter (16). These results suggest that EGF-ErbB and NRG-ErbB signaling play different roles in oligodendrocytes. However, the possible synergistic effects of overactivating NRG-ErbB and EGF-ErbB receptors in oligodendrocytes have not been investigated.

To understand the consequences of co-activating ErbB receptors in oligodendrocytes, we employed a pan-ErbB strategy and activated endogenous ErbB receptors mediating either NRG or EGF signaling in oligodendrocytes. The results demonstrated that

overactivating ErbB receptors in oligodendrocytes caused deleterious outcomes in white matter. Further, with the finding that the two inducible mouse tools, *Plp*-tTA and *Sox10*$^{+/rtTA}$, differentially targeted MO and OPC-NFO stages, we demonstrated that ErbB overactivation induced primary MO necroptosis and OPC apoptosis, causing demyelination and hypomyelination, respectively.

Results

ErbB overactivation caused demyelination in *Plp*-ErbB2^{V664E} mice

To manipulate ErbB receptor activities specifically in oligodendrocytes *in vivo*, we employed tetracycline-controlled systems whose induction or blockade depends on the presence of doxycycline (Dox). We generated *Plp*-tTA;*TRE*-ErbB2^{V664E} (*Plp*-ErbB2^{V664E}) bi-transgenic mice by crossing *Plp*-tTA with *TRE*-ErbB2^{V664E} mice. Breeding pairs, as well as their offspring, were fed with Dox to 'Tet-off' the *TRE*-controlled transcription. Dox was withdrawn when the offspring were weaned on P21 (Fig. 1A). Among ErbB1-4 receptors, ErbB2 that does not bind to any known ligand is the preferred partner to other ligand-bound ErbB members. ErbB2^{V664E} contains an amino acid mutation (Vla$_{664}$/Glu$_{664}$) within the transmembrane domain facilitating its dimerization with other ErbB receptors and potentiating their downstream signaling (21). Notably, *Plp*-ErbB2^{V664E} mice around P35 exhibited severe ataxia while walking on a grid panel (Fig. 1B). Moreover, *Plp*-ErbB2^{V664E} mice showed difficulty in rolling over, indicating severely impaired motor

coordination. This was unexpected as this phenotype has not been reported for NRG1- or hEGFR-overexpressing mice (16, 20).

With the expression and phosphorylation of ectopic ErbB2^{V664E}, endogenous ErbB receptors (EGFR, ErbB3 and ErbB4) were strikingly phosphorylated and activated in the white matter of *Plp*-ErbB2^{V664E} mice (Fig. 1, C and D). Activating ErbB receptors stimulated downstream signaling including both Erk (MAPK) and Akt that had phosphorylation increased in the white matter of *Plp*-ErbB2^{V664E} mice (Fig. 1, C and D).

Overactivation of ErbB receptors caused lower myelin staining intensity as exhibited in the corpus callosum of *Plp*-ErbB2^{V664E} mice at 9 days post Dox-withdrawal (dpd) after Luxol fast blue (LFB) staining (Fig. 1, E and F). White matter tracts in the lateral part of corpus callosum of *Plp*-ErbB2^{V664E} mice at 9 dpd were obviously fragmented (black arrows). Notably, at 14 dpd, myelin loss became more evident throughout the corpus callosum, as that LFB staining intensities dropped dramatically in both the middle and lateral parts (Fig. 1, E and F), suggesting that *Plp*-ErbB2^{V664E} mice were undergoing CNS demyelination after Dox withdrawal. Consistently, western blotting revealed loss of myelin basic protein (MBP), an indicator for MOs and myelin, in multiple brain regions of *Plp*-ErbB2^{V664E} mice (Fig. 1G). Moreover, the electron microscopic (EM) examination of the myelin ultrastructure revealed that myelin sheaths of some axons in *Plp*-ErbB2^{V664E} mice ruptured or underwent breakdown (Fig. 1, H, J, and K), consistent with the idea of demyelination. Due to demyelination, only a few intact axons were detected in the midline of the corpus callosum of *Plp*-ErbB2^{V664E} mice at 14 dpd (Fig. 1, J and K). When axonal tracts in the corpus callosum of *Plp*-ErbB2^{V664E} mice at 14 dpd were immunostained by TuJ1, the antibody recognizing neuronal specific β-tubulin III, the immunoreactivity

dramatically reduced (Fig. 1I). In addition, as a pathological condition, demyelination is usually complicated and aggravated by the pathological responses from nearby astrocytes and microglia. Indeed, in the white matter of *Plp*-ErbB2^{V664E} mice, astrogliosis and microgliosis were revealed (Fig. 1, L and M).

Plp-ErbB2^{V664E} white matter exhibited hypermyelination prior to demyelination

Interestingly, despite the demyelination, the detectable axons, throughout the corpus callosum, optic nerve, and prefrontal cortex in *Plp*-ErbB2^{V664E} mice, were hypermyelinated (Fig. 1J). Myelinated axons detected in the brain of *Plp*-ErbB2^{V664E} mice had significantly smaller *g*-ratio (axon diameter/fiber diameter), a quantitative indication of myelin thickness for individual axons with different diameters (Fig. 1J). Myelin thickness showed no difference between *TRE*-ErbB2^{V664E} and littermate *Plp*-tTA mice after Dox withdrawal (Fig. S1A). Therefore, hypermyelination of detectable axons in *Plp*-ErbB2^{V664E} mice was a result of the overexpression of ErbB2^{V664E}, which was detected by an antibody against ErbB2 (Fig. 1, C and G).

Hypermyelination of individual axons in *Plp*-ErbB2^{V664E} mice phenocopied that observed in NRG1-overexpressing mice (16). Overactivation of ErbB receptors transduce more active intracellular signaling than transduction through the increase of ligands. It is possible that the demyelination in *Plp*-ErbB2^{V664E} mice was a consequence of overproduction of myelin in MOs. If so, hypermyelination should occur prior to demyelination in *Plp*-ErbB2^{V664E} mice. We immunostained MBP in *Plp*-ErbB2^{V664E} mice, and found that myelin structures and distributions remained mostly normal in the middle part of corpus callosum at 9 dpd (Fig. 2A, inset 2' *vs* inset 2), despite that MBP loss and

myelin fragmentation were prominent at the cortical projection tips in the same mice (Fig. 2, A and C). An examination of the ultrastructure in these mice by EM revealed similar results that most axons were intact in the midline of the corpus callosum, although they have been significantly hypermyelinated (Fig. 2, B and D). These results confirmed that hypermyelination occurred early in *Plp*-ErbB2^{V664E} mice, and demyelination and axonal degeneration were pathological events induced secondarily by continuous ErbB activation.

ErbB overactivation induced oligodendrocyte degeneration but OPC regeneration in *Plp*-ErbB2^{V664E} mice

To investigate the pathological mechanism, we examined the post-mitotic oligodendrocytes by immunostaining with antibody CC1, and found a decreasing number of intact CC1^{+} cells in the corpus callosum of *Plp*-ErbB2^{V664E} mice starting from 6 dpd (Fig. 3, A and D). Meanwhile, OPC (NG2^{+}Olig2^{+}) numbers were dramatically increased in the white matter of *Plp*-ErbB2^{V664E} mice (Fig. 3, B to D). These disproportionate oligodendrocyte lineage state changes consolidated that the pathogenesis occurred in white matter, given that demyelination induces OPC regeneration (8, 20). We examined OPC proliferation by co-immunostaining for Olig2 and Ki67, the proliferation marker. In normal condition after early development, most proliferative OPCs (Ki67^{+}Olig2^{+}) resided in the subventricular zone, with a few in the trunk of corpus callosum (Fig. 3E). In *Plp*-ErbB2^{V664E} mice starting from 6 dpd, dramatic proliferation of OPCs was observed within the trunk of corpus callosum instead of the subventricular zone (Fig. 3, E and F), indicating that the pathogenetic factor was released in the myelin-enriched region.

ErbB overactivation caused oligodendrocyte number reduction and hypomyelination in *Sox10*-ErbB2^{V664E} mice

Next, we examined the effects of ErbB overactivation on CNS myelin by a 'Tet-on' system generated in *Sox10*$^{+/rtTA}$;*TRE*-ErbB2^{V664E} (*Sox10*-ErbB2^{V664E}) mice (Fig. 4A). *Sox10*-ErbB2^{V664E} mice with Dox feeding from P21 developed severe motor dysfunction, including ataxia and tremors, and died around P35. As a result, *Sox10*-ErbB2^{V664E} and littermate control mice were investigated at P30 after 9 days with Dox-feeding (dwd). These mice had smaller body sizes at P30 and walked with difficulty on a grid panel (Fig. 4B). Interestingly, *Sox10*-ErbB2^{V664E} mice performed normal rolling over. Despite walking slowly in the grid walking test, *Sox10*-ErbB2^{V664E} mice did not exhibit as many foot slips as *Plp*-ErbB2^{V664E} mice did. On the other hand, *Plp*-ErbB2^{V664E} mice did not exhibit tremors, which was possibly caused by the peripheral nerve deficiency in *Sox10*-ErbB2^{V664E} mice.

Western blotting revealed the expression and phosphorylation of ectopic ErbB2^{V664E} accompanied with increases in phosphorylation of ErbB3 and ErbB4, but not that of EGFR, in the white matter of *Sox10*-ErbB2^{V664E} mice (Fig. 4, C and D). Even though only the activities of ErbB3 and ErbB4, the receptors to the NRG family ligands, were increased in the white matter of *Sox10*-ErbB2^{V664E} mice, both downstream Erk and Akt signaling were activated (Fig. 4, C and D). With the ErbB signaling overactivation, brain slices stained by LFB exhibited lower staining intensity in the white matter of *Sox10*-ErbB2^{V664E} mice (Fig. 4, F and G), consistent with the lower MBP levels detected by western blotting (Fig. 4, C and E). Unexpectedly, the examination of the ultrastructure of *Sox10*-ErbB2^{V664E} white matter by EM did not find hypermyelination or myelin breakdown, but revealed that the

axons in the corpus callosum and optic nerve exhibited thinner myelin with significantly increased *g*-ratio (Fig. 4H). *Sox10*$^{+/rtTA}$ is a knock-in mouse line, so that the allele with *Sox10*-rtTA would not transcribe *Sox10* mRNA (22). We analyzed the ultrastructure of myelinated axons in *Sox10*$^{+/rtTA}$ and littermate *TRE*-ErbB2^{V664E} mice at P30 with 9 dwd and did not observe any differences (Fig. S1B). Therefore, we can exclude the possible effect of haploinsufficiency of Sox10 on late postnatal myelin development.

It is notable that in *Sox10*-ErbB2^{V664E} mice, the numbers of myelinated axons were not altered (Fig. 4I), and myelin sheaths exhibited normal morphology (Fig. 4H). Moreover, neither microgliosis nor astrogliosis was detected (Fig. 4, J and K). Because there was no indication of inflammatory pathogenesis, we can conclude that thinner myelin in *Sox10*-ErbB2^{V664E} white matter was caused by developmental deficits not pathological conditions. Therefore, ErbB overactivation in *Sox10*-ErbB2^{V664E} mice induced CNS hypomyelination rather than demyelination.

We further examined the states of oligodendrocytes and found the numbers of Olig2^{+}, NG2^{+}, and CC1^{+} cells all significantly decreased in the corpus callosum of *Sox10*-ErbB2^{V664E} mice (Fig. 4, L and M). The number reduction of NG2^{+} and CC1^{+} cells was proportional to each other and to that of Olig2^{+} cells, confirming that the deficits in *Sox10*-ErbB2^{V664E} mice were development-dependent. As no OPC or oligodendrocyte differences were observed between *Sox10*$^{+/rtTA}$ and *TRE*-ErbB2^{V664E} littermates at P30 with 9 dwd (Fig. S2, A and B), the developmental deficits in *Sox10*-ErbB2^{V664E} mice should be attributed to ErbB overactivation in oligodendrocytes.

Plp-tTA targeted mainly MOs whereas _Sox10_$^{+/rtTA}$ targeted OPC-NFOs during late postnatal development

The finding that _Plp_-ErbB2^{V664E} and _Sox10_-ErbB2^{V664E} mice had few overlapping phenotypes was unexpected considering that Sox10 is reported to express throughout the oligodendrocyte lineage, and _Sox10_$^{+/rtTA}$ knock-in mice have been used to investigate all oligodendrocyte lineage cells (23). On the other hand, _Plp_-tTA transgenic mice have been reported to target MOs in the adult brain (24); however, _Plp_ gene transcribes a shorter splicing isoform DM20 in OPCs and NFOs during embryonic and early postnatal development (25). Because the induction of the 'Tet-on' or 'Tet-off' system by Dox feeding or Dox withdrawal has a delayed effect on gene expression, and reporter proteins could accumulate to label the consecutive cellular stages, the results obtained by using _TRE_-controlled reporter mice fail to accurately reveal the original cells targeted by tTA or rtTA. To circumvent the shortcoming that reporter-containing cells observed in reporter mice may have highly deviated from their original states, we acutely delivered a _TRE_-controlled fluorescence reporter carried by an adeno-associated virus (AAV) into the mouse brains at P14 or P35, and examined tTA- or rtTA-targeted cells as well as their derivatives within 2 days.

Plp-tTA mice were raised with no Dox feeding, whereas _Sox10_$^{+/rtTA}$ were fed with Dox for 3 days before the stereotactic injection (Fig. 5A). One or 2 days after virus injection, the reporter-containing (YFP^{+}) cells were all immunopositive for Olig2 in both mouse lines at either age (Fig. S3, A to D), confirming their oligodendrocyte lineage specificity. To analyze the differentiation stage specificity, we immunostained AAV-_TRE_-YFP infected brain slices with an antibody for NG2 or PDGFRα that labels OPCs, or the antibody CC1

that labels post-mitotic oligodendrocytes. The results showed that very few (4-7%) YFP^+ cells were OPCs, while 92-97% of them were post-mitotic oligodendrocytes in *Plp*-tTA mice 1 or 2 days after virus injection at either age (Fig. 5, B and C, and Fig. S3, B and D). In the case of *Sox10*$^{+/rtTA}$ mice at P14, little difference was observed as only 5-6% of YFP^+ cells were OPCs 1 or 2 days after virus injection (Fig. 5B and Fig. S3A). However, for *Sox10*$^{+/rtTA}$ mice at P35, approximately 26% of YFP^+ cells were OPCs 1 day after virus injection (Fig. 5C and Fig. S3C). This observation excluded the possibility that the low OPC percentages in the reporter-containing cells in *Sox10*$^{+/rtTA}$ mice at P14, or in *Plp*-tTA mice at both ages, were due to selective infection by AAV. More intriguingly, the OPC/YFP^+ cell ratio decreased to 8% after 1 more day in *Sox10*$^{+/rtTA}$ mice at P35 (Fig. 5C). It is known that OPCs can differentiate into NFOs as quickly as 2.5 hours (5). These results may suggest that most of the pulse-labeled OPCs in *Sox10*$^{+/rtTA}$ mice at P35 were undergoing terminal differentiation (tOPCs), and *Sox10*$^{+/rtTA}$ increasingly targeted tOPCs from P14 to P35.

In most cases from *Sox10*$^{+/rtTA}$ mice, we noticed the total numbers of $NG2^+YFP^+$ (or $PDGFR\alpha^+YFP^+$) and $CC1^+YFP^+$ cells were fewer than that of $Olig2^+YFP^+$ cells (Fig. 5, B and C), which indicated the presence of targeted cells that were neither positive for CC1 nor for NG2 (PDGFRα). These cells belong to the NFO stage, which includes both $CC1^-NG2^-$ (or $CC1^-PDGFR\alpha^-$) and $CC1^+NG2^-$ (or $CC1^+PDGFR\alpha^-$) oligodendrocyte lineage cells. The β-catenin effector TCF4 is specifically expressed in the NFO stage (26-28), which was present in a subset of $Olig2^+$ cells but absent in $PDGFR\alpha^+$ cells in mice at P30 (Fig. 5D). In *Sox10*$^{+/rtTA}$ mice at P14, immunostaining revealed that approximately 49% of YFP^+ cells were NFOs ($TCF4^+$) 1 day after virus injection, but it reduced to 28% after 1

more day (Fig. 5, E and G). $TCF4^+$ cells found in the corpus callosum at P35 were far fewer than P14, and these cells appeared as clusters (Fig. S3E). Interestingly, in *Sox10*$^{+/rtTA}$ mice at P35, YFP^+ cells were mostly found in regions with $TCF4^+$ cell clusters (Fig. S3E), where approximately 56% of YFP^+ cells were $TCF4^+$ 1 day after virus injection and it reduced to 29% after 1 more day (Fig. 5, F and G). The half reduction of NFO percentage in YFP^+ cells from day 1 to day 2 was consistent with the previous report that NFOs mature into MOs in 1 or 2 days (5). There was another possibility that the transcriptional activity of *Sox10*-rtTA was low in MOs, and thus took more days to have detectable YFP levels. We analyzed the densities of $TCF4^+YFP^+$ cells and found that they reduced to half from day 1 to day 2 after viral infection in *Sox10*$^{+/rtTA}$ mice at either P14 or P35 (Fig. 5H). This result excluded the possibility that the reduction of NFO ratio in YFP^+ cells was due to the increase of targeted MOs, and confirmed the maturation rate of pulse-labeled NFOs from day 1 to day 2. A similar transition rate is applicable for targeted NFOs from day 0 to day 1. Therefore, the results that a high percentage (~50%) of YFP^+ cells were $TCF4^+$ at day 1 after viral infection corroborate that, from P14 to P35, the majority of cells targeted by *Sox10*$^{+/rtTA}$ at day 0 were tOPCs and NFOs (Fig. 5I).

AAV-*TRE*-YFP in *Plp*-tTA mice also labeled some $TCF4^+$ cells, which comprised only 7-12% of YFP^+ cells 1 or 2 days after virus injection at either age (Fig. 5, E to H). It was noticeable that *Plp*-tTA did not specifically target $TCF4^+$ cell clusters in the corpus callosum at P35 (Fig. S3F). These results implied that *Plp*-tTA did not specifically target the tOPC or the NFO stage but randomly expressed in the OPC-NFO period at a low ratio. Conversely, 90% of the YFP^+ cells were $TCF4^-$ and 92-97% were $CC1^+$ in *Plp*-tTA mice

at either P14 or P35, suggesting that *Plp*-tTA steadily targeted MOs after early development (Fig. 5I).

ErbB overactivation caused MO necroptosis whereas OPC apoptosis

With an understanding of the differentiation stage-specific targeting preferences of *Sox10*$^{+/rtTA}$ and *Plp*-tTA mice, we investigated the cellular mechanisms that determine the different myelin responses in *Plp*-ErbB2^{V664E} and *Sox10*-ErbB2^{V664E} mice. MO number reduction occurred earlier than the time when demyelination was obviously observed in the corpus callosum of *Plp*-ErbB2^{V664E} mice, suggesting oligodendropathy may be the cause of demyelination. We noticed there was an increase in the numbers of nuclei associated with CC1^{+} cell debris, starting from 6 dpd, in the corpus callosum of *Plp*-ErbB2^{V664E} mice (Fig. 3B, white arrows). We examined the corpus callosum of *Plp*-ErbB2^{V664E} mice by TdT-mediated dUTP nick end labeling (TUNEL) assay, and observed as little apoptotic signaling as that in controls (Fig. 6, A to C). This result revealed that the degenerating CC1^{+} cells were necrotic rather than apoptotic. Consistently, the oligodendrocyte nuclei associated with the destroyed myelin sheaths in *Plp*-ErbB2^{V664E} mice were regular nuclei without apoptotic chromatin condensation (Fig. 1H, red asterisk). In support of this theory, MLKL, the protein mediating oligodendrocyte necroptosis in multiple sclerosis (29) as well as the peripheral myelin breakdown after nerve injury (30), demonstrated an increased expression in the callosal CC1^{+} cells in *Plp*-ErbB2^{V664E} mice from 6 dpd (Fig. 6, D to F). Necroptosis is a programmed form of necrosis, and has been revealed to be a prominent pathological hallmark of multiple sclerosis (29). RIP3 is the kinase at the upstream of MLKL in this programmed death signaling pathway (29, 31).

Notably, the expression of RIP3 was also elevated in the callosal $CC1^+$ cells in *Plp*-ErbB2^{V664E} mice from 6 dpd as revealed by both immunostaining and western blotting (Fig. 6, D to F). Based on the timeline, MO necroptosis was the primary defect induced in *Plp*-ErbB2^{V664E} mice, followed by myelin breakdown, OPC regeneration, axonal degeneration, and other pathological events as reported in multiple sclerosis (8, 29).

In contrast, for *Sox10*-ErbB2^{V664E} mice, a dramatic increase in cell apoptosis ($TUNEL^+$) in the corpus callosum was observed (Fig. 6, C, G, and H). These apoptotic nuclei were localized in the $NG2^+$ cells (Fig. 6I), indicating apoptosis of OPCs. On the other hand, no increase of MLKL or RIP3 was detected (Fig. 6, E, F, and J), indicating there was no necroptosis. Developmental apoptosis does not arouse local inflammation, and hence no pathological responses were observed in astrocytes and microglia in the white matter of *Sox10*-ErbB2^{V664E} mice (Fig. 4, J and K). It is also interesting to note that both the $NG2^+$ cells with and without $TUNEL^+$ nuclei were hypertrophic in *Sox10*-ErbB2^{V664E} mice (Fig. 6I). This phenomenon was not revealed for $NG2^+$ cells in *Plp*-ErbB2^{V664E} mice (Fig. 3B), further supporting the different oligodendrocyte stage-targeting preferences of *Sox10*$^{+/rtTA}$ and *Plp*-tTA mice.

Discussion

The findings that the histological and cellular responses in *Sox10*-ErbB2^{V664E} and *Plp*-ErbB2^{V664E} mice were completely different consolidate the concept that *Sox10*$^{+/rtTA}$ and *Plp*-tTA target different oligodendrocyte stages during the late postnatal development. The MO-targeting preference of *Plp*-tTA mice was as expected and consistent with the previous

report (24). However, the finding that *Sox10*$^{+/rtTA}$ targeted OPC-NFO stages was not expected because *Sox10*$^{+/rtTA}$ mice were previously reported to target the whole oligodendrocyte lineage during early development as well as in adulthood (23). The previous report for *Sox10*$^{+/rtTA}$-targeting specificity was concluded by using reporter mice with Dox treatment for several weeks, in which the reporter-containing cells that included the *Sox10*$^{+/rtTA}$-targeting cells and their progeny were generated at different time. Moreover, the previous report only examined the immunoreactivities of reporter-containing cells to PDGFRα/NG2 and CC1. It is known that most NFOs are also positive for CC1 immunostaining (28). In our AAV-*TRE*-YFP-infecting mice, rtTA- or tTA-targeting cells were pulse-labeled, allowing us to analyze their differentiation stage transition rate. In *Sox10*$^{+/rtTA}$ mice 1 day after viral infection at P35, 26% cells labeled by the reporter proteins were positive for NG2 while 76% for CC1 (Fig. 5C), close to the previous report that in the reporter-containing cells induced by Dox in adult reporter mice, 27% were NG2^{+} and 65% were CC1^{+} (23). However, it is non-negligible that about 50% of reporter-containing cells at day 1 after viral infection in *Sox10*$^{+/rtTA}$ mice were TCF4^{+} (Fig. 5, E to G), indicating that many of the CC1^{+} cells were NFOs at this time. NFOs mature and lose their characteristic gene expression in 1 or 2 days (5). Through analyses of the stage alteration rate of reporter-containing cells from day 1 to day 2 after viral infection, we can conclude that the *Sox10*$^{+/rtTA}$-targeting cells at day 0 should mostly be tOPCs and NFOs (Fig. 5, E to H). Therefore, the reporter pulse-labeling results in *Sox10*$^{+/rtTA}$ and *Plp*-tTA mice and the distinct phenotypes in *Sox10*-ErbB2^{V664E} and *Plp*-ErbB2^{V664E} mice supported each other, and further substantiate that *Sox10*$^{+/rtTA}$ and *Plp*-tTA mice are valuable tools for *in vivo*

exploration of molecular and cellular mechanisms that involve oligodendrocyte development and pathogenesis after early development.

The advantages of *Sox10*$^{+/rtTA}$ and *Plp*-tTA mice that helped manipulate ErbB activities in non-overlapping oligodendrocyte lineage cells enabled us to distinguish the histological and cellular responses induced by activating ErbB receptors in MOs and OPC-NFOs, respectively. By analyzing *Plp*-ErbB2^{V664E} mice, we revealed that ErbB overactivation was pathogenetic in MOs through inducing MO necroptosis (Fig. 6, A to F), which led to demyelination followed by pathological changes including OPC regeneration, astrogliosis, microgliosis, and axonal degeneration (Figs. 1-3). Interestingly, studies on genetically modified mice that overexpressed hEGFR in oligodendrocyte lineage cells or overexpressed NRG1 in neurons did not report myelin pathogenesis (16, 20). Nevertheless, mice with overactivation of the ErbB downstream signaling in oligodendrocyte lineage cells exhibit myelin and axonal pathology. *Olig2*-Cre;Pten$^{flox/flox}$ mice that overactivate PI3K/Akt signaling in oligodendrocyte lineage cells have loosened myelin lamellae in the spinal cord at 14 weeks and axonal degeneration in the cervical spinal cord fasciculus gracilis at 62 weeks (32). *Plp*-CreER;Mek/Mek mice, which overexpress a constitutively activated MEK, a MAPK kinase, in oligodendrocyte lineage cells with tamoxifen induction, have demyelination in the spinal cord 3 months after the induction of MAPK (Erk) overactivation (33). A dose-dependent detrimental effect is suggested to MEK given the fact that *Plp*-CreER;+/Mek mice exhibit only hypermyelination but not demyelination even 8 months after induction. However, it should be noted that half dose of MEK overactivation also induces astrogliosis and microgliosis, two pathological symptoms in the CNS, in the spinal cord 8 months after induction (33), indicating that pathogenetic events might have

been sporadically occurred in the white matter of *Plp*-CreER;+/Mek mice. Devastating effects of ErbB2^{V664E} in *Plp*-ErbB2^{V664E} mice may be due to its potent promotion of endogenous ErbB activation and multiple downstream signaling including both PI-3K/Akt and MAPK (Erk) pathways (Fig. 1, C and D). There may be a dose-dependent effect for timing or severity of the pathological responses; however, observations in *Plp*-ErbB2^{V664E}, *Olig2*-Cre;Pten$^{flox/flox}$, and *Plp*-CreER;Mek/Mek mice corroborate the concept that continuously activating ErbB signaling in oligodendrocyte lineage cells is pathogenetic, even though it may take a long time for moderate activation to result in pathological symptoms. Given the fact that *Plp*-CreER and Olig2-Cre mice target the full oligodendrocyte lineage including OPCs (18), the cellular mechanism for the myelin pathogenesis in the previous reports was not determined. With the benefit of *Sox10*$^{+/rtTA}$ mice that mainly target OPC-NFOs after early development, we demonstrated that ErbB overactivation in OPCs induced apoptosis, leading to hypomyelination rather than inflammatory pathogenesis (Figs. 4 and 6). The differences in *Plp*-ErbB2^{V664E} and *Sox10*-ErbB2^{V664E} mice demonstrated that ErbB overactivation in MOs, but not OPC-NFOs, is pathogenetic.

It is intriguing that ErbB receptor overactivation in MOs and OPCs induced distinct deleterious effects. Because that RIP3 and MLKL, the core components of necroptotic machinery, increased specifically in MOs (Fig. 6D), but not astrocytes or microglia which were also pathologically activated in *Plp*-ErbB2^{V664E} white matter (Fig. 1, L and K), the necroptosis signaling pathway should be activated by intracellular signaling pathways downstream of ErbB receptors in MOs. Caspase-8 activation has been reported to be the key event to determine apoptotic fate of cells (34), and defective activation of caspase-8 is

critical for RIP1/RIP3/MLKL signaling to induce oligodendrocyte necroptosis in multiple sclerosis (29). A cell-type specific RNA-sequencing transcriptome analysis suggests that caspase-8 is minimally expressed in post-mitotic oligodendrocytes but is detectable in OPCs (35), which may determine MO necroptosis but OPC apoptosis under continuous ErbB activation. Thus, it will be worth pursuing whether caspase-8 is at the downstream of ErbB signaling and whether it is differentially expressed and activated in OPCs and MOs.

The demyelinating disease is now a broad concept that embraces more than multiple sclerosis, neuromyelitis optica, and leukodystrophy. Increasing evidence points to the correlation of the common demyelinating diseases with psychological symptoms (36, 37). On the other hand, white matter lesion is an emerging feature that can be examined periodically by structural brain imaging in patients with psychiatric disorders (13, 38). Remarkably, elevated ErbB activation has been repeatedly implicated in schizophrenia. For example, the mRNA and protein levels of NRG1 and ErbB4 are reported to increase in the prefrontal cortex and hippocampus of schizophrenic patients (39-41). These increases could be caused by genetic factors, such as schizophrenia-linked single nucleotide-polymorphisms (SNPs) SNP8NRG221132 and SNP8NRG243177, which are identified to increase the mRNA levels of NRG1 (41). In addition to increased expression, it has been shown that the capacity for ErbB4 to be activated is markedly improved in the prefrontal cortex of schizophrenic patients (42). Besides NRG1 and ErbB4 that have received extensive attention, EGFR is observed to increase in the brain of some schizophrenic patients (43).

The white matter abnormalities observed in our mouse models are reminiscent of diverse myelin-related clinical characteristics in schizophrenic brains, including reduced

white matter volume, decreased oligodendrocyte densities, reduced myelin gene products, apoptotic oligodendrocytes, and damaged myelin (38, 44-47). To our knowledge, we are the first to reveal that ErbB overactivation can primarily induce oligodendropathy and myelin pathogenesis in white matter, providing a possible predisposition of a genetic variability in the ErbB receptors or ligands to the white matter lesion. Notably, SNP8NRG243177 with T-allele, which increases NRG1 Type IV production (41), is associated with the reduced white matter integrity in schizophrenic patients (48). The direct evidence provided by the present study that gain of function in ErbB receptors causes primary white matter lesions emphasizes that monitoring white matter in live patients and testing the genetic variability of ErbB signaling pathways are two necessary methods to help develop prognostic and therapeutic strategies for psychiatric disorders.

Intrinsic genetic alterations, apart from the pathogenetic immune responses, may also cause primary oligodendropathy in multiple sclerosis (49). Oligodendrocyte necroptosis has been revealed to be a hallmark in multiple sclerosis (29), indicating that ErbB receptor activation is possible an upstream pathogenic mechanism for the most common demyelinating disease. It has been reported that inhibition of MAPK (Erk) activity by PD0325901, a MEK inhibitor, promotes OPC differentiation and myelin regeneration in two different animal models of the demyelinating disease (50). Moreover, an EGF antibody has been used to neutralize EGF in the animal model of multiple sclerosis and exhibits therapeutic effects by promoting oligodendrogenesis and ameliorating pathological status (51). Therefore, our findings provide a novel molecular insight into the primary oligodendropathy in demyelinating diseases, and support that a strategy targeting ErbB overactivation may be beneficial in the therapy of the diseases.

Materials and Methods

Animals. *Plp*-tTA transgenic mice were from the RIKEN BioResource Center (Stock No. RBRC05446). Transgenic mice *TRE*-ErbB2^{V664E} (Stock No. 010577) was from the Jackson Laboratory. Sox10$^{+/rtTA}$ mice were from Dr. Michael Wegner (University Erlangen-Nurnberg, Germany). Unless indicated, mice were housed in a room with a 12-hour light/dark cycle with access to food and water *ad libitum*. For biochemical and histological experiments, *Plp*-tTA;*TRE*-ErbB2^{V664E} (*Plp*-ErbB2^{V664E}) and *Sox10*$^{+/rtTA}$;*TRE*-ErbB2^{V664E} (*Sox10*-ErbB2^{V664E}) mice with either sex and their littermate control mice with matched sex were used. Animal experiments were approved by the Institutional Animal Care and Use Committee of the Hangzhou Normal University. For genotyping, the following primers were used: for *Plp*-tTA (630bp), PLPU-604 5'-TTT CCC ATG GTC TCC CTT GAG CTT, mtTA24L 5'-CGG AGT TGA TCA CCT TGG ACT TGT; for Sox10$^{+/rtTA}$ (618bp), sox10-rtTA1 5'-CTA GGC TGT CAG AGC AGA CGA, sox10-rtTA2 5'-CTC CAC CTC TGA TAG GT CTT G; for *TRE*-ErbB2^{V664E} (625bp), 9707 5'-AGC AGA GCT CGT TTA GTG, 9708 5'-GGA GGC GGC GAC ATT GTC.

Tet-Off or Tet-On treatment of mice. Mice with Tet-system contain genes of tetracycline-controlled transcriptional activator (tTA) or reverse tetracycline-controlled transcriptional activator (rtTA) driven by cell-specific promoters. When fed with Dox, these mice are able to switch on or off expression of a gene under the control of *tetracycline-responsive element* (*TRE*), specifically in rtTA- or tTA-expressing cells, which are called 'Tet-on' or 'Tet-off', respectively. The offspring of *Sox10*$^{+/rtTA}$ during the indicated periods were fed with Dox (2 mg/mL × 10 mL/day from P21 to indicated test

day) in drinking water to induce the expression of ErbB2^{V664E} in *Sox10*-ErbB2^{V664E} mice (Tet-On). For the offspring of *Plp*-tTA, Dox was given (Tet-off) from the embryonic day (through pregnant mothers) to their weaning day at P21 to inhibit the expression of ErbB2^{V664E} during this period in *Plp*-ErbB2^{V664E} mice (0.5 mg/mL × 10 mL/day of Dox before P21). Water bottles were wrapped with foil to protect Dox from light. All used littermate control mice were treated the same.

Stereotaxic injection of AAV viruses. pAAV-*TRE*-EYFP plasmids (Addgene) were packaged as AAV2/9 viruses, and produced with titers of 2.0E+13 particles per mL by OBio (Shanghai, China). Mice were anesthetized by 1% pentobarbital (50 mg/kg, i.p.) and mounted at stereotaxic apparatus (RWD68025). AAV-*TRE*-EYFP (2 μL) was injected into the corpus callosum (from bregma in mm, M-L: ±1.2, A-P: +0.5, D-V: -2.2) under the control of micropump (KDS310) at a speed of 0.05 μL/min. Injecting needles (Hamilton NDL ga33/30 mm/pst4) were withdrawn 10 min after injection. Infected brains were isolated 1 or 2 days later and brain slices were immunostained with anti-GFP antibody to enhance the visualization of the reporter protein.

Electron Microscopy. Mice were anesthetized and transcardially perfused with 4% sucrose, 4% paraformaldehyde (PFA) and 2% glutaraldehyde in 0.1 M phosphate buffer (PB, pH 7.4). The brains and optic nerves were isolated carefully. The corpora callosa and prefrontal cortices were further dissected carefully under stereoscope. Tissues were post-fixed overnight at 4°C in 1% glutaraldehyde in 0.1 M PB. 24 hr later, samples were washed by 0.1 M PB and osmicated with 2% osmium tetroxide 30-60 min at 4°C, washed by 0.1

M PB and by deionized H_2O at 4°C, and dehydrated in graded (50-100%) ethanol. Samples were incubated with propylene oxide and embedded with embedding resins. Ultrathin sections were stained with 2% uranyl acetate at 4°C for 30 min, and then photographed with Tecnai 10 (FEI). EM images were analyzed by ImageJ (NIH). To eliminate the bias on circularity, *g*-ratio of each axon was calculated by the perimeter of axons (inner) divided by the perimeter of corresponding fibers (outer). Axonal diameters were normalized by perimeters through equation: diameter = perimeter/π. This procedure allows for inclusion of irregularly shaped axons and fibers and helps to eliminate biased measurement of diameters based on circularity. For quantitative analysis, cross sections of each neural tissue were divided into 5 areas, and more than two images, randomly selected from each area, were examined.

Immunofluorescence staining. Deeply anesthetized mice were transcardially perfused with 0.01 M PBS and then 4% PFA in 0.01 M PBS. Mouse brains were isolated and post-fixed in 4% PFA in 0.01 M PBS overnight at 4 °C, and then transferred into 20% and subsequently 30% sucrose in PBS overnight at 4 °C. Brains were then embedded in OCT (Thermo Fisher scientific) and sectioned into 20 μm on a cryostat sectioning machine (Thermo Fisher scientific, Microm HM525). Brain slices were incubated with a blocking buffer (10% fetal bovine serum and 0.2% Triton-X-100 in 0.01 M PBS) for 1 hr at room temperature (RT), and then incubated at 4 °C overnight with primary antibodies diluted in the blocking buffer. The primary antibodies used were: GFP (1:500, Abcam, ab13970), CC1 (1:500, Abcam, ab16794), NG2 (1:200, Abcam, ab50009), Ki67 (1:400, Cell Signaling Technology, 9129), GFAP (1:2000, Millipore, MAB360), Iba1 (1:1000,

Millipore, MABN92), MBP (1:100, Millipore, MAB382), TCF4 (1:500, Millipore, 05-511), Olig2 (1:500, Millipore, AB9610), TUJ1 (1:500, Sigma, T5076), RIP3 (1:500, QED, 2283), MLKL (1:500, Abgent, AP14272B). After washing three times with 0.1% Triton-X-100 in 0.01 M PBS, samples were incubated at RT for 1 hr with Alexa-488 or -594 secondary antibody, and then washed and mounted on adhesion microscope slides (CITOTEST) with fluorescent mounting medium. Nuclear labeling was completed by incubating slices with DAPI (0.1 μg/mL, Roche) at RT for 5 min after incubation with secondary antibodies. Except for the antibody against NG2, antigen retrieval in 0.01 M sodium citrate buffer (pH 6.0) at 80-90 °C for 10 min was necessary before primary antibody incubation for brain slices to achieve definitive signals. Images were taken by a Zeiss LSM710 confocal microscope or a Nikon Eclipse 90i microscope. For cell counting based on immunostaining results, soma-shaped immunoreactive signals associated with a nucleus was counted as a cell. The immunostaining intensity was measured by ImageJ with background subtraction. For MBP distribution analysis, images were applied with a threshold to eliminate the background, and the percentage of signal area in the total area was quantified as the signal distribution and normalized to that of controls.

Luxol fast blue (LFB) staining. Brain slices were obtained as described in Immunofluorescence staining. After sufficient washing with 0.01 M PBS, the slices were transferred into a mixture of trichloromethane and ethanol (volume ratio 1:1) for 10 min and then 95% ethanol for 10 min. They were next incubated in 0.2% Luxol fast blue staining solution (0.2 g Solvent blue 38, 0.5 mL acetic acid, 95% ethanol to 100 mL) at 60 °C overnight. The next day, tissues were incubated for 5 min each in turn in 95% ethanol,

70% ethanol and ddH_2O for rehydration, followed by incubation alternatively in 0.05% Li_2CO_3, 70% ethanol and ddH_2O for differentiation until the contrast between the gray matter and white matter became obvious. After that, tissues were incubated for 10 min each in 95% and 100% ethanol to dehydrate, and then 5 min in dimethylbenzene to clear, before quickly mounting with neutral balsam mounting medium (CWBIO). All steps were operated in a ventilation cabinet. The LFB intensity in the corpus callosum was measured by Image J with background subtraction, and normalized to that of controls.

TUNEL assay. Apoptotic cells were examined with terminal deoxynucleotidyl transferase (TdT)-mediated deoxyuridine triphosphate (dUTP) nick-end labeling (TUNEL) assay according to the manufacturer's instructions (Vazyme; Yeasen). In brief, brain slices which were obtained as that described in Immunofluorescence staining were digested for 10 min by proteinase K (20 μg/mL) at RT. After washing twice with PBS, brain slices were incubated with Equilibration Buffer for 30 min at RT, and subsequently with Alexa Fluor 488-12-dUTP Labeling Mix for 60 min at 37°C. After washing with PBS three times, brain slices were stained with DAPI before being mounted under coverslips. For co-labeling of apoptotic nuclei in slices with immunofluorescence staining, TUNEL assay was performed after washing of the secondary antibody.

Western blotting. Subcortical white matter tissues were isolated and homogenized. Homogenates in lysis buffer (10 mM Tris-Cl, pH 7.4, 1% NP-40, 0.5% Triton-X 100, 0.2% sodium deoxycholate, 150 mM NaCl, 20% glycerol, protease inhibitor cocktail) at a ratio of 2 mL per 100 mg tissue were lysed overnight in 4°C. Lysates were centrifuged at 12,000

g and 4°C for 15 min to get rid of the unsolved debris. Concentration of the supernatant was measured by BCA assay. Proteins in samples were separated by 6-12% SDS-PAGE, transferred to a Immobilon-P Transfer Membrane (Millipore), and then incubated with indicated primary antibodies diluted in blocking buffer at 4°C overnight after blocking by 5% non-fat milk solution in TBST (50 mM Tris, pH 7.4, 150 mM NaCl, 0.1% Tween 20) for 1 hr at RT. The primary antibodies used were: pErbB3 (1:2500, Abcam, ab133459), pErbB4 (1:2500, Abcam, ab109273), pErbB2 (1:2500, Abgent, AP3781q), EGFR (1:5000, Epitomics, 1902-1), pEGFR (1:2500, Epitomics, 1727-1), GAPDH (1:5000, Huabio, EM1101), MBP (1:1000, Millipore, MAB382), ErbB3 (1:200, Santa Cruz Biotechnology, sc-285), ErbB4 (1:200, Santa Cruz Biotechnology, sc-283), ErbB2 (1:200, Santa Cruz Biotechnology, sc-284), Akt (1:5000, Cell signaling Technology, 9272), pAkt (1:3000, Cell signaling Technology, 9271), Erk1/2 (1:5000, Cell signaling Technology, 9102), pErk1/2 (1:5000, Cell signaling Technology, 4370), RIP3 (1:2000, QED, 2283), MLKL (1:2000, Abgent, AP14272B). For antibodies against phosphorylated proteins, 10% fetal bovine serum was used as a blocking buffer. Next day, the membranes were washed by TBST for three times and incubated with the secondary antibodies for 1 hr at RT. Membranes were washed again and incubated with Immobilon Western Chemiluminescent HRPSubstrate (Millipore) for visualization of chemiluminescence by exposure to X-ray films or Bio-Rad GelDOCXR^{+} Imaging System. Intensities of protein bands were measured by ImageJ, and statistical analysis was performed after subtraction of the background intensity and normalization with controls in each batch of experiments.

Statistical Analysis. All data were analyzed using Prism (Graphpad) and presented as mean ± s.e.m.. Unpaired two-tailed Student's *t* test was used for analysis between two groups with one variable. Statistical significance was set at $*P < 0.05$, $**P < 0.01$, $***P < 0.001$.

Acknowledgments

We thank Haiping Xiong, Wanwan He, Kaiwei Zhang, Youguang Yang, and Shasha Zhang in Hangzhou Normal University for the assistance in EM image analyses. This work was supported by grants from the National Natural Science Foundation of China (31371075, 31671070, and 31871030 to YT).

Author contributions: Y.T. conceived, designed and supervised research; X.H., G.X., L.H., X.N., H.L., Q.X., and Z.W. performed experiments; M.Q., K.T. and Y.S. provided technique support; X.H., G.X., L.H., X.N., H.L., and Y.T. analyzed data; Y.T. wrote the paper. All authors have read and approved the manuscript.

Competing interests: The authors declare no competing interests.

References

1. D. E. Bergles, W. D. Richardson, Oligodendrocyte Development and Plasticity. *Cold Spring Harb Perspect Biol* **8**, a020453 (2015).
2. B. Emery, Q. R. Lu, Transcriptional and Epigenetic Regulation of Oligodendrocyte

Development and Myelination in the Central Nervous System. *Cold Spring Harb Perspect Biol* **7**, a020461 (2015).

3. T. Czopka, C. Ffrench-Constant, D. A. Lyons, Individual oligodendrocytes have only a few hours in which to generate new myelin sheaths in vivo. *Dev Cell* **25**, 599-609 (2013).
4. T. A. Watkins, B. Emery, S. Mulinyawe, B. A. Barres, Distinct stages of myelination regulated by gamma-secretase and astrocytes in a rapidly myelinating CNS coculture system. *Neuron* **60**, 555-569 (2008).
5. L. Xiao *et al.*, Rapid production of new oligodendrocytes is required in the earliest stages of motor-skill learning. *Nat Neurosci* **19**, 1210-1217 (2016).
6. R. B. Tripathi *et al.*, Remarkable Stability of Myelinating Oligodendrocytes in Mice. *Cell Rep* **21**, 316-323 (2017).
7. E. G. Hughes, J. L. Orthmann-Murphy, A. J. Langseth, D. E. Bergles, Myelin remodeling through experience-dependent oligodendrogenesis in the adult somatosensory cortex. *Nat Neurosci* **21**, 696-706 (2018).
8. M. Bradl, H. Lassmann, Oligodendrocytes: biology and pathology. *Acta Neuropathol* **119**, 37-53 (2010).
9. K. K. Bercury *et al.*, Conditional ablation of raptor or rictor has differential impact on oligodendrocyte differentiation and CNS myelination. *J Neurosci* **34**, 4466-4480 (2014).
10. A. I. Flores *et al.*, Akt-mediated survival of oligodendrocytes induced by neuregulins. *The Journal of neuroscience : the official journal of the Society for Neuroscience* **20**, 7622-7630 (2000).

11. A. I. Flores *et al.*, Constitutively active Akt induces enhanced myelination in the CNS. *J Neurosci* **28**, 7174-7183 (2008).
12. A. Ishii, S. L. Fyffe-Maricich, M. Furusho, R. H. Miller, R. Bansal, ERK1/ERK2 MAPK signaling is required to increase myelin thickness independent of oligodendrocyte differentiation and initiation of myelination. *J Neurosci* **32**, 8855-8864 (2012).
13. L. Mei, K. A. Nave, Neuregulin-ERBB signaling in the nervous system and neuropsychiatric diseases. *Neuron* **83**, 27-49 (2014).
14. K. A. Nave, J. L. Salzer, Axonal regulation of myelination by neuregulin 1. *Curr Opin Neurobiol* **16**, 492-500 (2006).
15. J. Schmucker *et al.*, erbB3 is dispensable for oligodendrocyte development in vitro and in vivo. *Glia* **44**, 67-75 (2003).
16. B. G. Brinkmann *et al.*, Neuregulin-1/ErbB signaling serves distinct functions in myelination of the peripheral and central nervous system. *Neuron* **59**, 581-595 (2008).
17. M. Makinodan, K. M. Rosen, S. Ito, G. Corfas, A critical period for social experience-dependent oligodendrocyte maturation and myelination. *Science* **337**, 1357-1360 (2012).
18. F. Guo, J. Ma, E. McCauley, P. Bannerman, D. Pleasure, Early postnatal proteolipid promoter-expressing progenitors produce multilineage cells in vivo. *J Neurosci* **29**, 7256-7270 (2009).
19. J. Palazuelos *et al.*, TACE/ADAM17 is essential for oligodendrocyte development and CNS myelination. *J Neurosci* **34**, 11884-11896 (2014).

20. A. Aguirre, J. L. Dupree, J. M. Mangin, V. Gallo, A functional role for EGFR signaling in myelination and remyelination. *Nat Neurosci* **10**, 990-1002 (2007).

21. J. Chen *et al.*, A role for ErbB signaling in the induction of reactive astrogliosis. *Cell Discov* **3**, 17044 (2017).

22. A. Ludwig, B. Schlierf, A. Schardt, K. A. Nave, M. Wegner, Sox10-rtTA mouse line for tetracycline-inducible expression of transgenes in neural crest cells and oligodendrocytes. *Genesis* **40**, 171-175 (2004).

23. A. Wegener *et al.*, Gain of Olig2 function in oligodendrocyte progenitors promotes remyelination. *Brain* **138**, 120-135 (2015).

24. N. Inamura *et al.*, Gene induction in mature oligodendrocytes with a PLP-tTA mouse line. *Genesis* **50**, 424-428 (2012).

25. B. D. Trapp, A. Nishiyama, D. Cheng, W. Macklin, Differentiation and death of premyelinating oligodendrocytes in developing rodent brain. *J Cell Biol* **137**, 459-468 (1997).

26. S. P. Fancy *et al.*, Dysregulation of the Wnt pathway inhibits timely myelination and remyelination in the mammalian CNS. *Genes Dev* **23**, 1571-1585 (2009).

27. H. Fu *et al.*, A genome-wide screen for spatially restricted expression patterns identifies transcription factors that regulate glial development. *J Neurosci* **29**, 11399-11408 (2009).

28. F. Ye *et al.*, HDAC1 and HDAC2 regulate oligodendrocyte differentiation by disrupting the beta-catenin-TCF interaction. *Nat Neurosci* **12**, 829-838 (2009).

29. D. Ofengeim *et al.*, Activation of necroptosis in multiple sclerosis. *Cell Rep* **10**, 1836-1849 (2015).

30. Z. Ying *et al.*, Mixed Lineage Kinase Domain-like Protein MLKL Breaks Down Myelin following Nerve Injury. *Mol Cell* **72**, 457-468 e455 (2018).

31. L. Sun *et al.*, Mixed lineage kinase domain-like protein mediates necrosis signaling downstream of RIP3 kinase. *Cell* **148**, 213-227 (2012).

32. E. P. Harrington *et al.*, Oligodendrocyte PTEN is required for myelin and axonal integrity, not remyelination. *Ann Neurol* **68**, 703-716 (2010).

33. A. Ishii, M. Furusho, J. L. Dupree, R. Bansal, Strength of ERK1/2 MAPK Activation Determines Its Effect on Myelin and Axonal Integrity in the Adult CNS. *J Neurosci* **36**, 6471-6487 (2016).

34. A. Oberst *et al.*, Catalytic activity of the caspase-8-FLIP(L) complex inhibits RIPK3-dependent necrosis. *Nature* **471**, 363-367 (2011).

35. Y. Zhang *et al.*, An RNA-sequencing transcriptome and splicing database of glia, neurons, and vascular cells of the cerebral cortex. *J Neurosci* **34**, 11929-11947 (2014).

36. C. Diaz-Olavarrieta, J. L. Cummings, J. Velazquez, C. Garcia de la Cadena, Neuropsychiatric manifestations of multiple sclerosis. *J Neuropsychiatry Clin Neurosci* **11**, 51-57 (1999).

37. N. D. Chiaravalloti, J. DeLuca, Cognitive impairment in multiple sclerosis. *Lancet Neurol* **7**, 1139-1151 (2008).

38. R. D. Fields, White matter in learning, cognition and psychiatric disorders. *Trends Neurosci* **31**, 361-370 (2008).

39. V. Z. Chong *et al.*, Elevated neuregulin-1 and ErbB4 protein in the prefrontal cortex of schizophrenic patients. *Schizophrenia research* **100**, 270-280 (2008).

40. D. Joshi, J. M. Fullerton, C. S. Weickert, Elevated ErbB4 mRNA is related to interneuron deficit in prefrontal cortex in schizophrenia. *Journal of psychiatric research* **53**, 125-132 (2014).

41. A. J. Law *et al.*, Neuregulin 1 transcripts are differentially expressed in schizophrenia and regulated by 5' SNPs associated with the disease. *Proceedings of the National Academy of Sciences of the United States of America* **103**, 6747-6752 (2006).

42. C. G. Hahn *et al.*, Altered neuregulin 1-erbB4 signaling contributes to NMDA receptor hypofunction in schizophrenia. *Nat Med* **12**, 824-828 (2006).

43. T. Futamura *et al.*, Abnormal expression of epidermal growth factor and its receptor in the forebrain and serum of schizophrenic patients. *Mol Psychiatry* **7**, 673-682 (2002).

44. G. Douaud *et al.*, Anatomically related grey and white matter abnormalities in adolescent-onset schizophrenia. *Brain* **130**, 2375-2386 (2007).

45. N. A. Uranova, O. V. Vikhreva, V. I. Rachmanova, D. D. Orlovskaya, Ultrastructural alterations of myelinated fibers and oligodendrocytes in the prefrontal cortex in schizophrenia: a postmortem morphometric study. *Schizophr Res Treatment* **2011**, 325789 (2011).

46. N. A. Uranova *et al.*, The role of oligodendrocyte pathology in schizophrenia. *Int J Neuropsychopharmacol* **10**, 537-545 (2007).

47. M. Hoistad *et al.*, Linking white and grey matter in schizophrenia: oligodendrocyte and neuron pathology in the prefrontal cortex. *Front Neuroanat* **3**, 9 (2009).

48. A. M. McIntosh *et al.*, The effects of a neuregulin 1 variant on white matter density and integrity. *Mol Psychiatry* **13**, 1054-1059 (2008).

49. D. C. Factor *et al.*, Cell Type-Specific Intralocus Interactions Reveal Oligodendrocyte Mechanisms in MS. *Cell* **181**, 382-395 e321 (2020).

50. N. Suo, Y. E. Guo, B. He, H. Gu, X. Xie, Inhibition of MAPK/ERK pathway promotes oligodendrocytes generation and recovery of demyelinating diseases. *Glia* **67**, 1320-1332 (2019).

51. Y. Amir-Levy, K. Mausner-Fainberg, A. Karni, Treatment with Anti-EGF Ab Ameliorates Experimental Autoimmune Encephalomyelitis via Induction of Neurogenesis and Oligodendrogenesis. *Mult Scler Int* **2014**, 926134 (2014).

Figure legends

Fig. 1. ErbB overactivation in *Plp*-ErbB2^{V664E} mice induced demyelination. (A) Dox treatment setting for indicated mice and littermate controls. (**B**) Walking speed and percentage of foot slips of *Plp*-ErbB2^{V664E} mice and littermate controls at P35 with 14 dpd in the grid walking test. Data were presented as mean ± s.e.m., and analyzed by unpaired *t* test. n = 4 mice for each group. For velocity, $t_{(6)} = 3.773$, $P = 0.0093$; For foot slips, $t_{(6)} = 12.31$, $P < 0.0001$. (**C**) Western blotting of indicated proteins in white matter tissues isolated from *Plp*-ErbB2^{V664E} (PB) mice in comparison with that from littermate control mice (Ctrl). Activation status of each ErbB receptor or downstream signaling protein was examined by western blotting with the specific antibody against its phosphorylated form. (**D**) Quantitative data of western blotting results were presented as mean ± s.e.m., and analyzed by unpaired *t* test. For EGFR, $t_{(4)} = 27.64$, $P < 0.0001$; for ErbB3, $t_{(4)} = 19.98$, $P < 0.0001$; for ErbB4, $t_{(4)} = 10.06$, $P = 0.00055$; for Akt, $t_{(4)} = 8.096$, $P = 0.0013$; for Erk, $t_{(4)} = 4.353$, $P = 0.012$. (**E**) LFB staining results of coronal sections through the genu of the corpus callosum in *Plp*-ErbB2^{V664E} and control mice. Black arrows indicate the lower staining intensity of myelin stained in the corpus callosum. (**F**) Quantitative data for LFB staining intensity in the corpus callosum of indicated mice. Data were presented as mean ± s.e.m. and analyzed by unpaired *t* *t*est. For the middle part at 9 dpd, $t_{(6)} = 6.345$, $P = 0.00072$; for the lateral part at 9 dpd, $t_{(6)} = 3.914$, $P = 0.0078$; for the middle part at 14 dpd, $t_{(6)} = 9.89$, $P < 0.0001$; for the lateral part at 14 dpd, $t_{(6)} = 23.07$, $P < 0.0001$. (**G**) Western blotting results of MBP and ErbB2 in multiple brain regions (CX, cortex; CE, cerebellum; SC, spinal cord; ME, medulla) isolated from *Plp*-ErbB2^{V664E} (PB) and littermate control

mice (Ctrl) at 14 dpd. GAPDH served as a loading control. Quantitative data were presented as mean ± s.e.m., and analyzed by unpaired *t* test. For CE, $t_{(4)} = 6.35$, $P = 0.0032$; for CX, $t_{(4)} = 9.243$, $P = 0.00076$; for SC, $t_{(4)} = 4.118$, $P = 0.0146$; for ME, $t_{(4)} = 3.634$, $P = 0.022$. (**H**) Representative EM images showed that myelin sheath ruptured and broke down in *Plp*-ErbB2^{V664E} mice at 14 dpd (red arrow). Note the associated nuclei (red asterisk) showed no chromatin condensation and nucleation. (**I**) Axons were reduced in the subcortical white matter (white arrows) of *Plp*-ErbB2^{V664E} mice at 14 dpd. Sagittal sections of *Plp*-ErbB2^{V664E} and littermate control mice were immunostained by monoclonal antibody TuJ1. Subcortical staining intensities were measured and plotted as mean ± s.e.m., and analyzed by unpaired *t* test. $t_{(4)} = 6.019$, $P = 0.0009$. (**J**) EM images of the corpus callosum (CC), optic nerve (ON), and prefrontal cortex (PFC) from *Plp*-ErbB2^{V664E} and littermate controls at 14 dpd. Quantitative data were shown for *g*-ratio analysis of myelinated axons detected by EM. Averaged *g*-ratio for each mouse were plotted as inset, presented as mean ± s.e.m., and analyzed by unpaired *t* test. For CC, $t_{(4)} = 3.412$, $P = 0.027$; for ON, $t_{(4)} = 3.083$, $P = 0.037$; for PFC, $t_{(4)} = 7.11$, $P = 0.0021$. Red arrow indicates the axon with myelin breakdown. (**K**) The densities of myelinated axons, as well as the percentages of axons with myelin breakdown, examined by EM in different brain regions of *Plp*-ErbB2^{V664E} (PB) and littermate control mice (Ctrl) at 14 dpd were quantified. Data were presented as mean ± s.e.m., and analyzed by unpaired *t* test. For myelinated-axon density, in CC, $t_{(4)} = 2.683$, $P = 0.046$; in ON, $t_{(4)} = 1.818$, $P = 0.143$. For the percentage of axons with myelin breakdown, in CC, $t_{(4)} = 29.32$, $P < 0.0001$; in ON, $t_{(4)} = 6.108$, $P = 0.0036$; in PFC, $t_{(4)} = 8.125$, $P = 0.0012$. (**L** and **M**) Astrocytes (GFAP^{+}) and microglia (Iba1^{+}) examined in the subcortical white matter of indicated mice by immunostaining.

Cell densities in the corpus callosum were quantified, and data were presented as mean ± s.e.m., and analyzed by unpaired *t* test. In L, $t_{(10)} = 4.753$, $P = 0.0008$. In M, $t_{(4)} = 36.4$, $P < 0.0001$.

Fig. 2. *Plp*-ErbB2^{V664E} white matter exhibited hypermyelination prior to demyelination. (**A**) MBP immunostaining of brain slices from indicated mice. Note the myelin structure and distribution exhibited relatively more normal in the middle part of corpus callosum (inset 2') than that in the layer II/III of cortex (inset 1'), in *Plp*-ErbB2^{V664E} mice at 9 dpd. (**B**) EM examination of axons in the midline of the corpus callosum (CC) and the prefrontal cortex (PFC) in *Plp*-ErbB2^{V664E} mice at 9 dpd. *g*-ratio was calculated for myelinated axons and averaged *g*-ratio were analyzed by unpaired *t* test (inset). For CC, $t_{(4)} = 3.226$, $P = 0.032$; for PFC, $t_{(4)} = 2.529$, $P = 0.065$. Red arrows indicate the axons with myelin breakdown. (**C**) Quantitative data of MBP signal distribution in immunostaining results. Data were presented as mean ± s.e.m., and analyzed by unpaired *t* test. In middle CC, $t_{(6)} = 13.11$, $P < 0.0001$; in cortex layer II/III, $t_{(6)} = 26.31$, $P < 0.0001$. (**D**) The densities of myelinated axons as well as the percentages of axons with myelin breakdown in EM analysis. Data were presented as mean ± s.e.m., and analyzed by unpaired *t* test. For myelinated-axon density in CC, $t_{(4)} = 0.805$, $P = 0.466$. For axons with myelin breakdown at 9 dpd examined by EM, In CC, $t_{(4)} = 3.567$, $P = 0.023$; in PFC, $t_{(4)} = 4.146$, $P = 0.014$.

Fig. 3. ErbB overactivation induced oligodendrocyte degeneration but OPC regeneration in *Plp*-ErbB2^{V664E} mice. (**A**) The numbers of degenerating oligodendrocytes (represented by nuclei associated with CC1$^+$ cell debris, white arrows) increased in the corpus callosum of *Plp*-ErbB2^{V664E} mice starting from 6 dpd as revealed by CC1 immunostaining. The densities of remained intact CC1$^+$ cells were reduced. (**B**) Immunostaining results of NG2 in the corpus callosum of indicated mice. (**C**) Dramatically increased Olig2$^+$ and NG2$^+$ cells in the subcortical white matter of *Plp*-ErbB2^{V664E} mice at 14 dpd. Sagittal sections of *Plp*-ErbB2^{V664E} and littermate control mice were immunostained by antibodies for Olig2 or NG2. (**D**) Quantitative data of immunostaining results in *Plp*-ErbB2^{V664E} (PB) and control mice (Ctrl) with indicated Dox treatment were present as mean ± s.e.m., and analyzed by unpaired *t* test. For CC1$^+$ density: at 4 dpd, $t_{(4)} = 1.485$, $P = 0.212$; for 6 dpd, $t_{(4)} = 5.203$, $P = 0.0065$; for 9 dpd, $t_{(4)} = 20.95$, $P < 0.0001$. For Olig2$^+$ density: at 4 dpd, $t_{(6)} = 0.2923$, $P = 0.780$; at 6 dpd, $t_{(6)} = 3.16$, $P = 0.0196$; at 9 dpd, $t_{(4)} = 8.563$, $P = 0.001$. For NG2$^+$ density at 9 dpd, $t_{(4)} = 9.912$, $P = 0.0006$. (**E**) Immunostaining results of Olig2 with Ki67 in the corpus callosum of indicated mice. (**F**) Quantitative data of Ki67$^+$Olig2$^+$ cell density in *Plp*-ErbB2^{V664E} (PB) and control mice (Ctrl) with indicated Dox treatment were present as mean ± s.e.m., and analyzed by unpaired *t* test. At 4 dpd, $t_{(4)} = 1.187$, $P = 0.301$; at 6 dpd, $t_{(4)} = 3.428$, $P = 0.027$; at 9 dpd, $t_{(4)} = 8$, $P = 0.0013$.

Fig. 4. ErbB overactivation induced oligodendrocyte number reduction and hypomyelination in *Sox10*-ErbB2^{V664E} mice. (**A**) Dox treatment setting for indicated

mice and littermate controls. (**B**) Walking speed and percentage of foot slips of *Sox10*-ErbB2^{V664E} mice and littermate controls at 9 dwd in the grid walking test. Data were presented as mean ± s.e.m., and analyzed by unpaired *t* test. n = 4 mice for each group. For velocity, $t_{(6)}$ = 3.504, P = 0.0128; For foot slips, $t_{(6)}$ = 4.429, P = 0.0044. (**C**) Western blotting of indicated proteins in white matter tissues isolated from *Sox10*-ErbB2^{V664E} (SB) mice in comparison with that from littermate control mice (Ctrl). Activation status of each ErbB receptor or downstream signaling protein was examined by western blotting with the specific antibody against its phosphorylated form. (**D** and **E**) Quantitative data of western blotting results were presented as mean ± s.e.m., and analyzed by unpaired *t* test. In D, for EGFR, $t_{(4)}$ = 0.1983, P = 0.852; for ErbB3, $t_{(4)}$ = 28.34, P < 0.0001; for ErbB4, $t_{(4)}$ = 9.181, P = 0.00078; for Akt, $t_{(4)}$ = 3.380, P = 0.028; for Erk, $t_{(4)}$ = 4.899, P = 0.008. In E, for MBP, $t_{(4)}$ = 48.82, P < 0.0001. (**F**) LFB staining results of coronal sections through the genu of the corpus callosum in *Sox10*-ErbB2^{V664E} (SB) and control mice (Ctrl). Black arrows indicate the lower staining intensity of myelin stained in the corpus callosum. (**G**) Quantitative data for LFB staining intensity in the corpus callosum of indicated mice. Data were presented as mean ± s.e.m. and analyzed by unpaired *t* test. For the middle part, $t_{(6)}$ = 15.17, P < 0.0001; for the lateral part, $t_{(6)}$ = 10.23, P < 0.0001. (**H**) EM images of the corpus callosum (CC), optic nerve (ON), and prefrontal cortex (PFC) from *Sox10*-ErbB2^{V664E} and littermate controls at 9 dwd. Quantitative data were shown for *g*-ratio analysis of myelinated axons detected by EM. Averaged *g*-ratio for each mouse were plotted as inset, presented as mean ± s.e.m., and analyzed by unpaired *t* test. For CC, $t_{(4)}$ = 3.295, P = 0.0301; for ON, $t_{(4)}$ = 3.775, P = 0.0195; for PFC, $t_{(4)}$ = 1.196, P = 0.298. (**I**) The densities of myelinated axons examined by EM in different brain regions of *Sox10*-ErbB2^{V664E} (SB)

and littermate control mice (Ctrl) at 9 dwd were quantified. Data were presented as mean ± s.e.m., and analyzed by unpaired *t* test. In CC, $t_{(4)} = 0.2773$, $P = 0.795$; in ON, $t_{(4)} = 0.1455$, $P = 0.891$. (**J** and **K**) Astrocytes ($GFAP^+$) and microglia ($Iba1^+$) examined in the subcortical white matter of indicated mice by immunostaining. Cell densities in the corpus callosum were quantified, and data were presented as mean ± s.e.m., and analyzed by unpaired *t* test. In J, $t_{(4)} = 0.0501$, $P = 0.962$. In K, $t_{(4)} = 1.637$, $P = 0.178$. (**L**) $Olig2^+$, $CC1^+$, and $NG2^+$ cells in the corpus callosum of indicated mice at indicated ages were examined by immunostaining. (**M**) Statistic results of $Olig2^+$, $CC1^+$, and $NG2^+$ cell densities in the corpus callosum of *Sox10*-$ErbB2^{V664E}$ (SB) mice and littermate controls (Ctrl) at P30 with 9 dwd. Data were from repeated immunostaining of 3 mice for each group, presented as mean ± s.e.m., and analyzed by unpaired *t* test. For $Olig2^+$, $t_{(4)} = 6.236$, $P = 0.0034$; for $CC1^+$, $t_{(4)} = 16.92$, $P < 0.0001$; for $NG2^+$, $t_{(4)} = 3.634$, $P = 0.0221$.

Fig. 5. *Plp*-tTA targeted MOs whereas *Sox10*$^{+/rtTA}$ targeted OPC-NFOs in mouse brains in late postnatal development. (**A**) Schematic illustration of stereotactic injection sites of AAV-*TRE*-YFP. (**B** and **C**) Percentage of $Olig2^+YFP^+$, $CC1^+YFP^+$, or $PDGFR\alpha^+YFP^+$ ($NG2^+YFP^+$) cells in YFP^+ cells for indicated mice 1 (AAV-1d) or 2 days (AAV-2d) after AAV-*TRE*-YFP injection at P14 (B) or P35 (C). Data were from repeated immunostaining results of 3-7 mice for each group, presented as mean ± s.e.m., and analyzed by unpaired *t* test. For *Plp*-tTA at P14 from AAV-1d to AAV-2d: $Olig2^+YFP^+$ cells, $t_{(12)} = 0.3698$, $P = 0.718$; $CC1^+YFP^+$ cells, $t_{(13)} = 0.5666$, $P = 0.581$; $PDGFR\alpha^+YFP^+$ cells, $t_{(10)} = 7.532$, $P < 0.0001$. For *Sox10*-rtTA at P14 from AAV-1d to AAV-2d:

Olig2^{+}YFP^{+} cells, $t_{(13)}$ = 0.2055, P = 0.840; CC1^{+}YFP^{+} cells, $t_{(8)}$ = 0.6425, P = 0.539; PDGFRα^{+}YFP^{+} cells, $t_{(5)}$ = 1.021, P = 0.354. For *Plp*-tTA at P35 from AAV-1d to AAV-2d: Olig2^{+}YFP^{+} cells, $t_{(17)}$ = 0.4959, P = 0.626; CC1^{+}YFP^{+} cells, $t_{(9)}$ = 2.32, P = 0.046; NG2^{+}YFP^{+} cells, $t_{(18)}$ = 1.003, P = 0.329. For *Sox10*-rtTA at P35 from AAV-1d to AAV-2d: Olig2^{+}YFP^{+} cells, $t_{(11)}$ = 1.098, P = 0.296; CC1^{+}YFP^{+} cells, $t_{(23)}$ = 0.8614, P = 0.398; NG2^{+}YFP^{+} cells, $t_{(26)}$ = 7.869, P < 0.0001. (**D**) Immunostaining revealed that TCF4 was specifically expressed in a small fraction of Olig2^{+} cells, but not in PDGFRα^{+} cells, in the corpus callosum of mice at P30. Solid arrow, representative double positive cell; Open arrow, representative cell positive for TCF4 only. (**E** and **F**) Double immunostaining results of TCF4 and YFP for brain slices from indicated mice 1 (AAV-1d) or 2 days (AAV-2d) after virus injection at P14 (E) or P35 (F). Note that TCF4^{+} nuclei in AAV-infected area were almost all localized in YFP^{+} cells in *Sox10*$^{+/rtTA}$ mice 1 day after virus injection (AAV-1d) at either P14 or P35, and the colocalization reduced after 1 more day (AAV-2d). Solid arrows, representative double positive cells; Open arrows, representative cells positive for TCF4 only. (**G** and **H**) The percentage of TCF4^{+}YFP^{+} in YFP^{+} cells (G), and the density of TCF4^{+}YFP^{+} cells (H), were analyzed. Data were from repeated immunostaining results of 3-7 mice for each group, presented as mean ± s.e.m., and analyzed by unpaired *t* test. For the percentage in *Plp*-tTA mice from AAV-1d to AAV-2d: at P14, $t_{(26)}$ = 1.574, P = 0.128; at P35, $t_{(22)}$ = 2.367, P = 0.027. For the percentage in *Sox10*$^{+/rtTA}$ mice from AAV-1d to AAV-2d: at P14, $t_{(10)}$ = 4.39, P = 0.0014; at P35, $t_{(28)}$ = 6.041, P < 0.0001. For the density in *Plp*-tTA mice from AAV-1d to AAV-2d: at P14, $t_{(26)}$ = 1.581, P = 0.126; at P35, $t_{(22)}$ = 1.429, P = 0.167. For the density in *Sox10*$^{+/rtTA}$ mice from AAV-1d to AAV-2d: at P14, $t_{(10)}$ = 5.685, P = 0.0002; at P35, $t_{(28)}$ = 4.813, P < 0.0001. (**I**)

Schematic summary of oligodendrocyte stage-targeting preferences of *Plp*-tTA or *Sox10*$^{+/rtTA}$ during juvenile to adolescent development.

Fig. 6. ErbB overactivation induced MO necroptosis in *Plp*-ErbB2^{V664E} mice but OPC apoptosis in *Sox10*-ErbB2^{V664E} mice. (**A** and **G**) Dox treatment setting for indicated mice and littermate controls. (**B** and **H**) Apoptotic cells (arrows) in the corpus callosum of *Plp*-ErbB2^{V664E} and control mice at 9 dpd (B), or *Sox10*-ErbB2^{V664E} and control mice at 9 dwd (H), were examined by TUNEL assays. Note the increased numbers of nuclei (DAPI^{+}) and non-specifically stained hemorrhagic spots (asterisk), which is the consequence of inflammation, in the brain slice of *Plp*-ErbB2^{V664E} mice (B). (**C**) Quantitative data of apoptotic cell densities in indicated mice. PB, *Plp*-ErbB2^{V664E}. SB, *Sox10*-ErbB2^{V664E}. Ctrl, control mice. Data were presented as mean ± s.e.m., and analyzed by unpaired *t* test. For PB, $t_{(6)} = 0.1128$, $P = 0.914$; for SB, $t_{(5)} = 8.344$, $P = 0.0004$. (**D** and **J**) Co-immunostaining results of MLKL or RIP3 with CC1 in the corpus callosum of indicated mice with indicated Dox treatments. (**E**) Western blotting results of MLKL and RIP3 in the white matter of *Plp*-ErbB2^{V664E} (PB) mice, or in that of *Sox10*-ErbB2^{V664E} (SB) mice, and in those of littermate control mice (Ctrl). ns, non-specific bands. (**F**) Quantitative data of immunostaining and western blotting results of MLKL or RIP3 in indicated mice at 9 days with Dox treatments. Data were presented as mean ± s.e.m., and analyzed by unpaired *t* test. In western blotting results, for RIP3 protein in PB, $t_{(4)} = 3.579$, $P = 0.023$; for MLKL protein in PB, $t_{(4)} = 13.69$, $P = 0.00017$. In immunostaining results, for percentage of RIP3^{+} in CC1^{+} cells in PB, $t_{(4)} = 6.002$, $P = 0.0039$; for percentage of MLKL^{+} in CC1^{+} cells in

PB, $t_{(4)} = 8.202$, $P = 0.0012$. (**I**) Apoptotic cells ($TUNEL^+$) were OPCs ($NG2^+$) in *Sox10*-$ErbB2^{V664E}$ mice at P30 with 9 dwd. Arrows, representative double positive cells. Note OPCs in *Sox10*-$ErbB2^{V664E}$ mice were hypertrophic. The percentage of $TUNEL^+NG2^+$ cells in $NG2^+$ cells were quantified and data were presented as mean ± s.e.m. and analyzed by unpaired *t* test. $t_{(4)} = 3.95$, $P = 0.0168$.

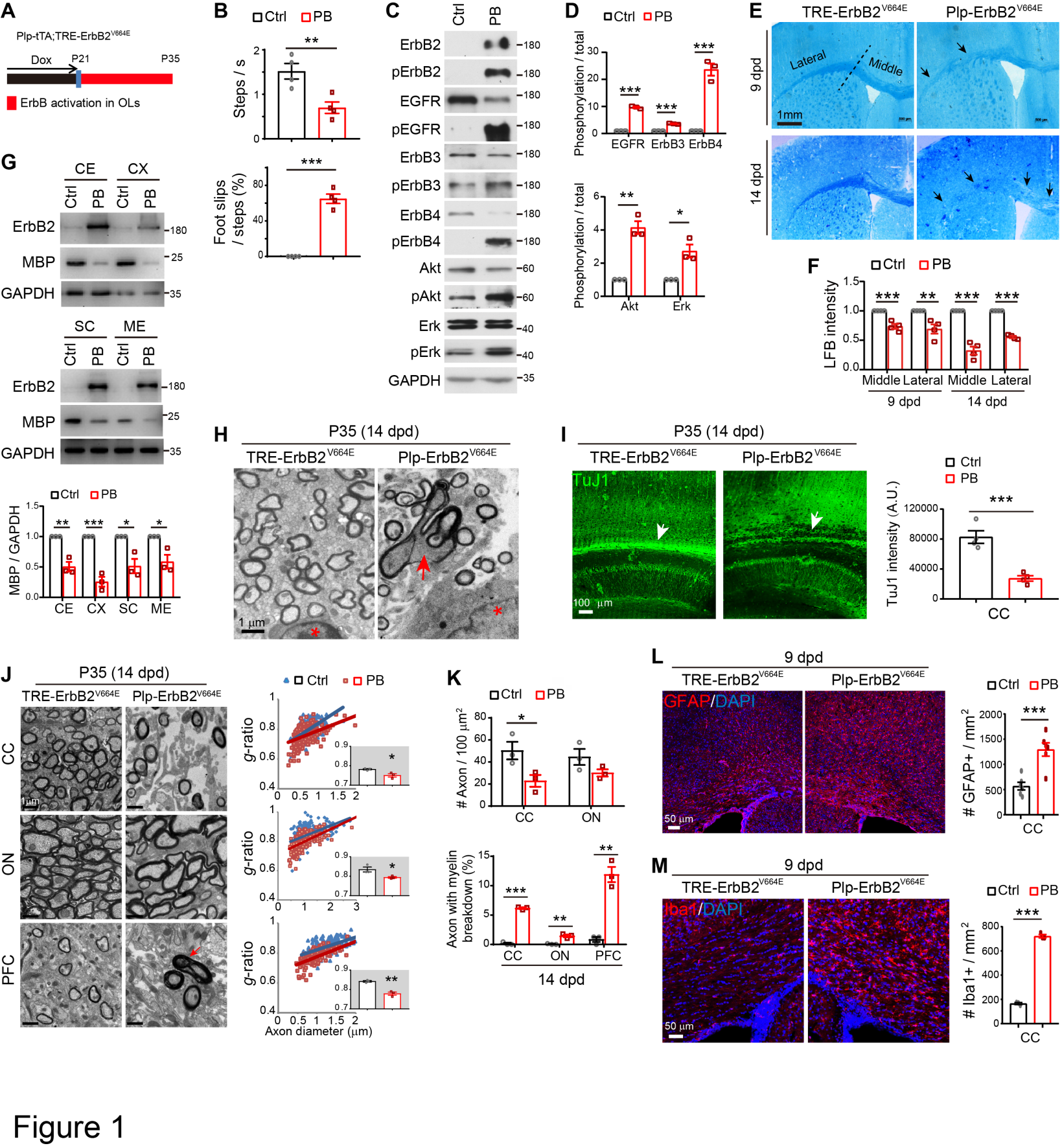
A
Plp-tTA;TRE-ErbB2V664E
Dox
P21
P35
ErbB activation in OLs
B
Ctrl
PB
Steps / s
Foot slips / steps (%)
C
ErbB2
pErbB2
EGFR
pEGFR
ErbB3
pErbB3
ErbB4
pErbB4
Akt
pAkt
Erk
pErk
GAPDH
D
Phosphorylation / total
EGFR
ErbB3
ErbB4
Akt
Erk
E
TRE-ErbB2V664E
Plp-ErbB2V664E
9 dpd
14 dpd
Lateral
Middle
1mm
F
LFB intensity
Middle
Lateral
9 dpd
14 dpd
G
CE
CX
SC
ME
MBP
MBP / GAPDH
H
P35 (14 dpd)
1 μm
I
TuJ1
100 μm
TuJ1 intensity (A.U.)
CC
J
CC
ON
PFC
g-ratio
Axon diameter (μm)
K
Axon / 100 μm2
Axon with myelin breakdown (%)
L
GFAP/DAPI
50 μm
GFAP+ / mm2
M
Iba1/DAPI
Iba1+ / mm2

Figure 1

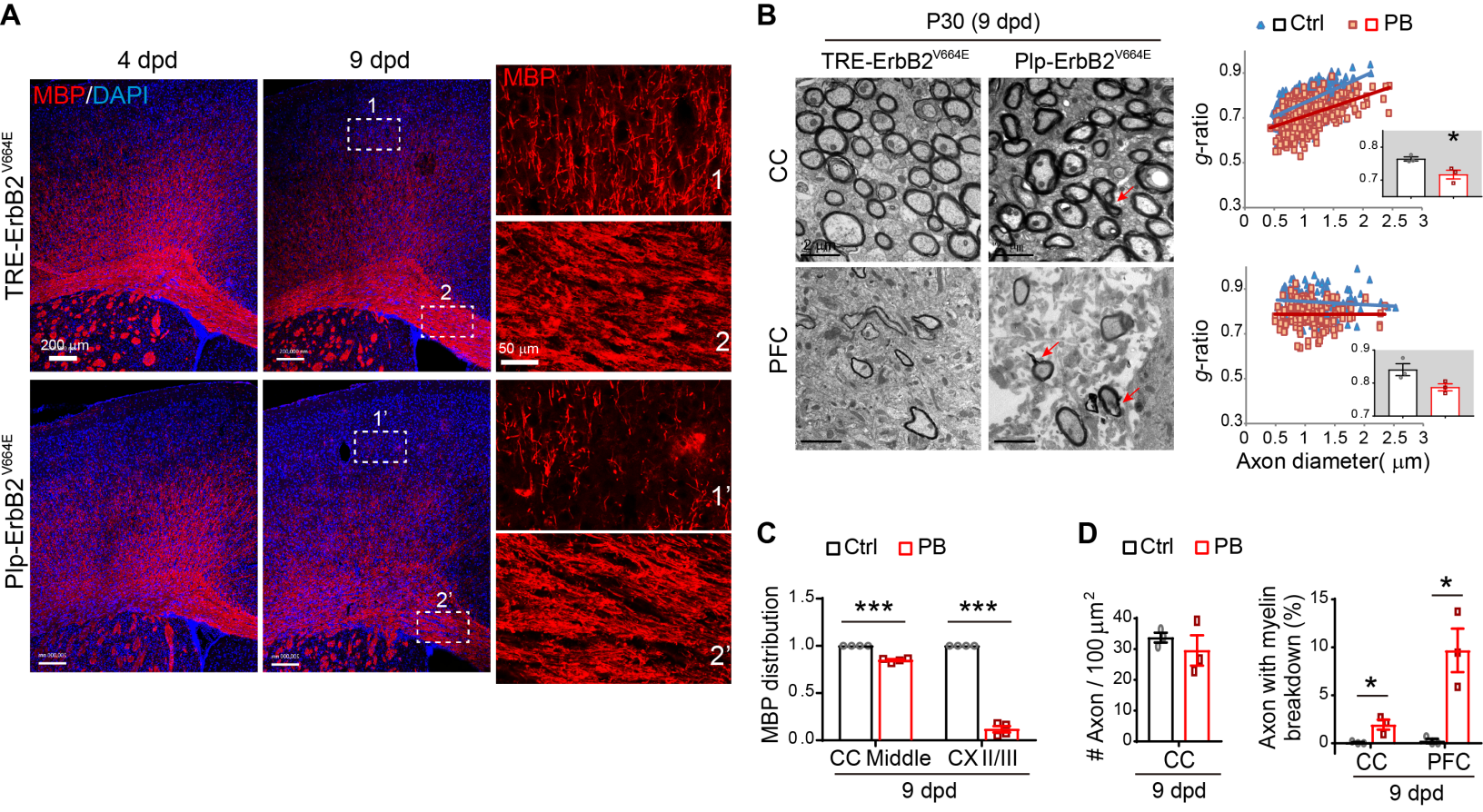
A
4 dpd
9 dpd
MBP/DAPI
MBP
TRE-ErbB2V664E
Plp-ErbB2V664E
200 μm
50 μm
1
2
1'
2'
B
P30 (9 dpd)
TRE-ErbB2V664E
Plp-ErbB2V664E
CC
PFC
Ctrl
PB
g-ratio
Axon diameter(μm)
C
MBP distribution
CC Middle
CX II/III
9 dpd
D
Axon / 100 μm2
Axon with myelin breakdown (%)
CC
PFC

Figure 2

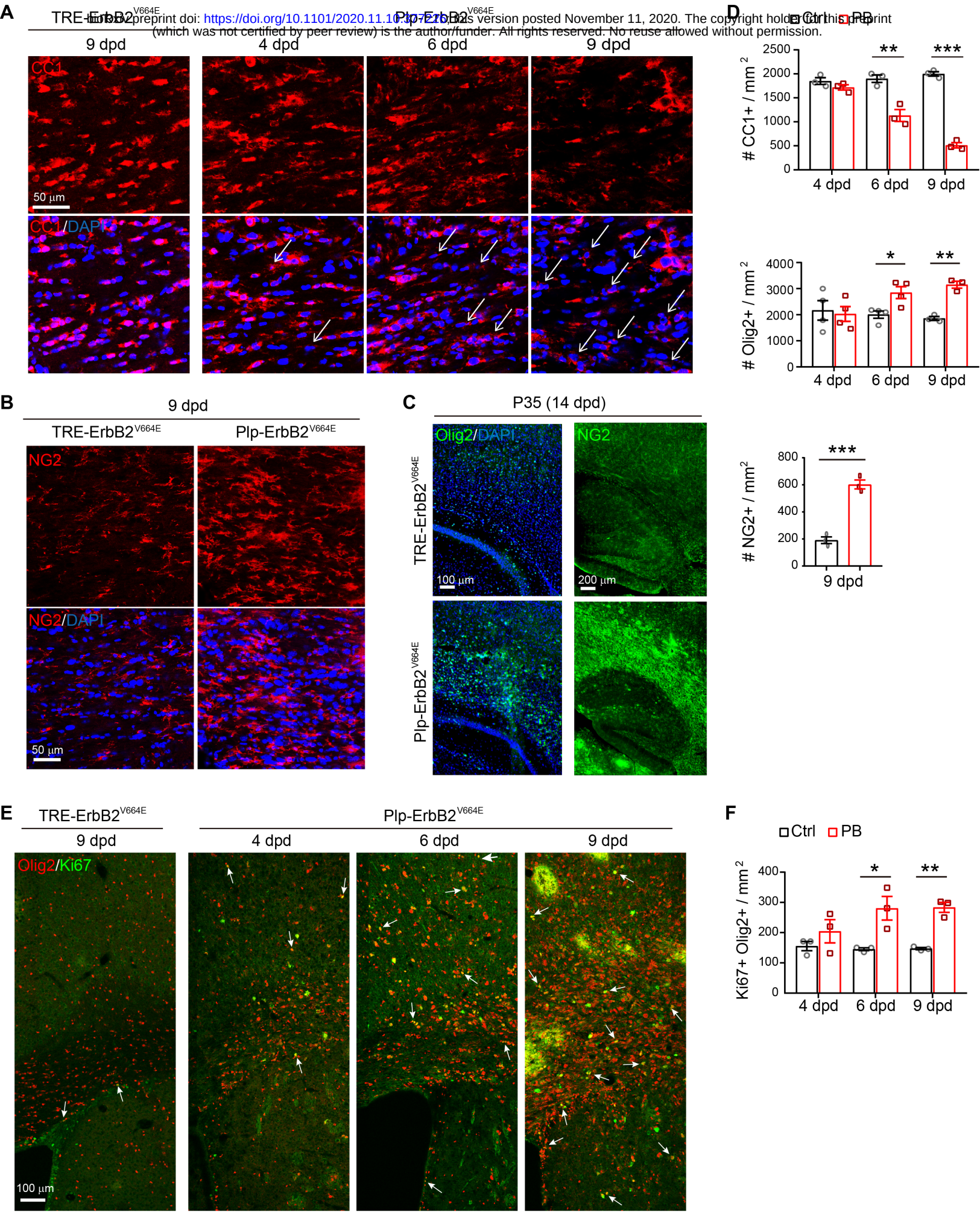

Figure 3

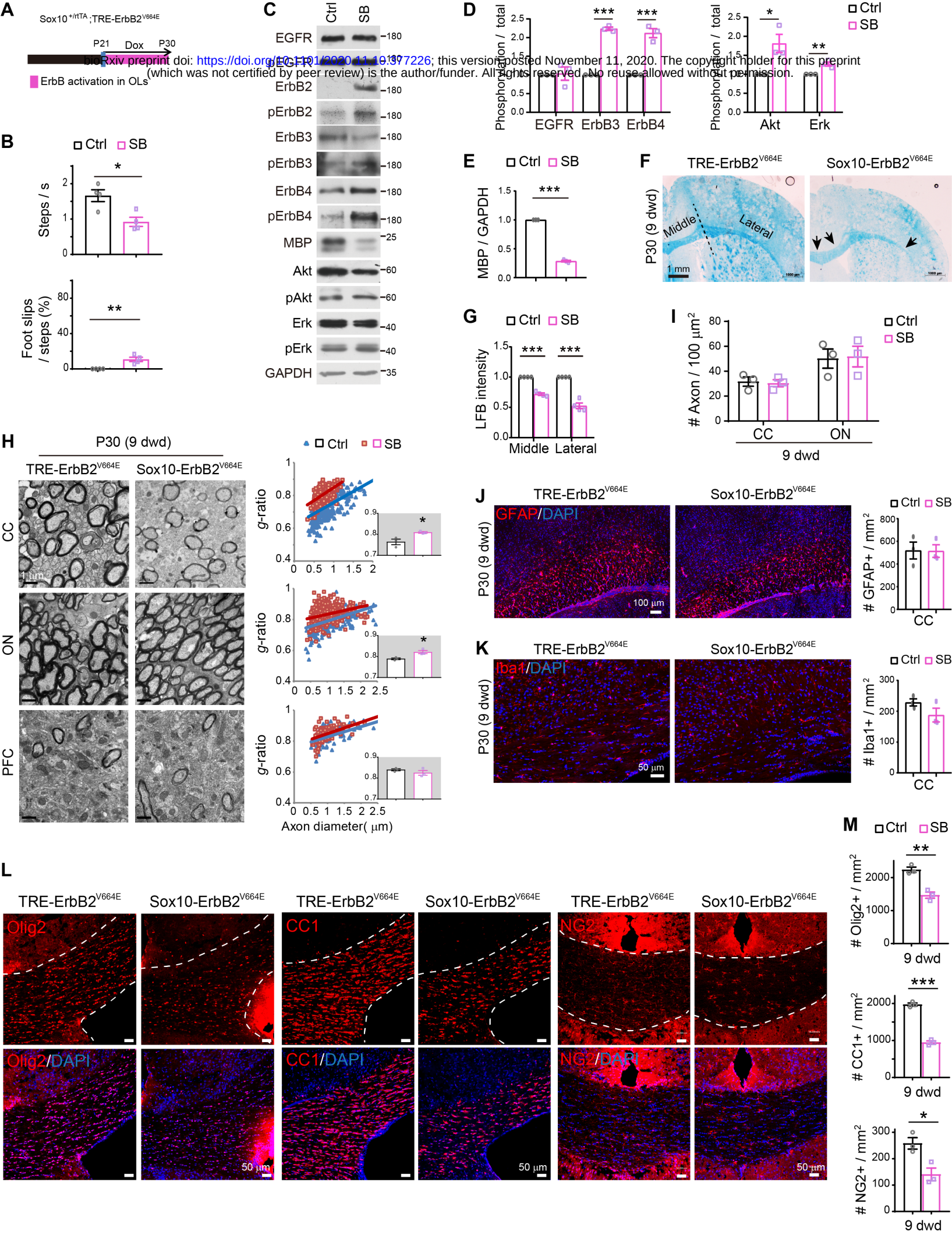

Figure 4

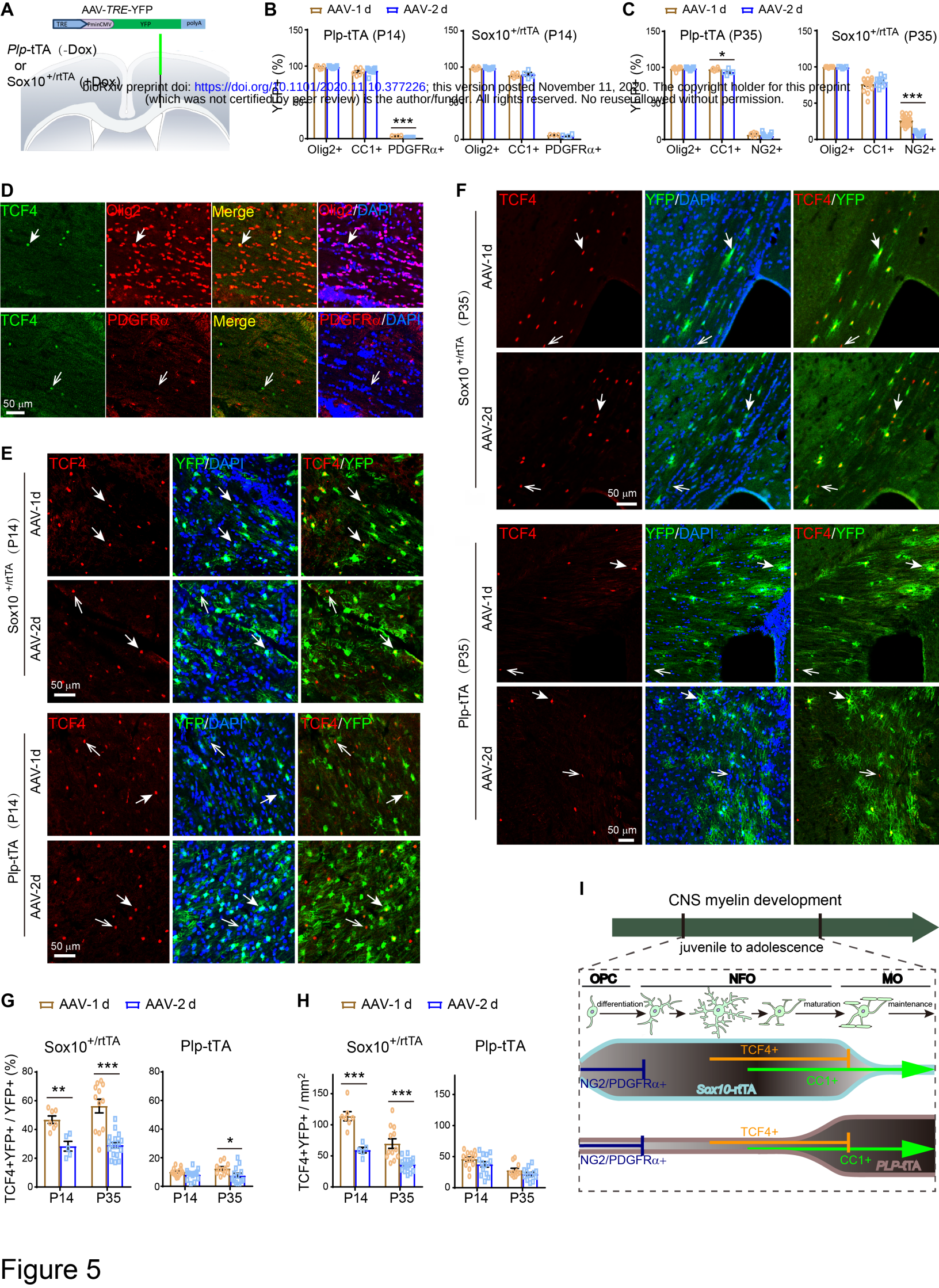

Figure 5

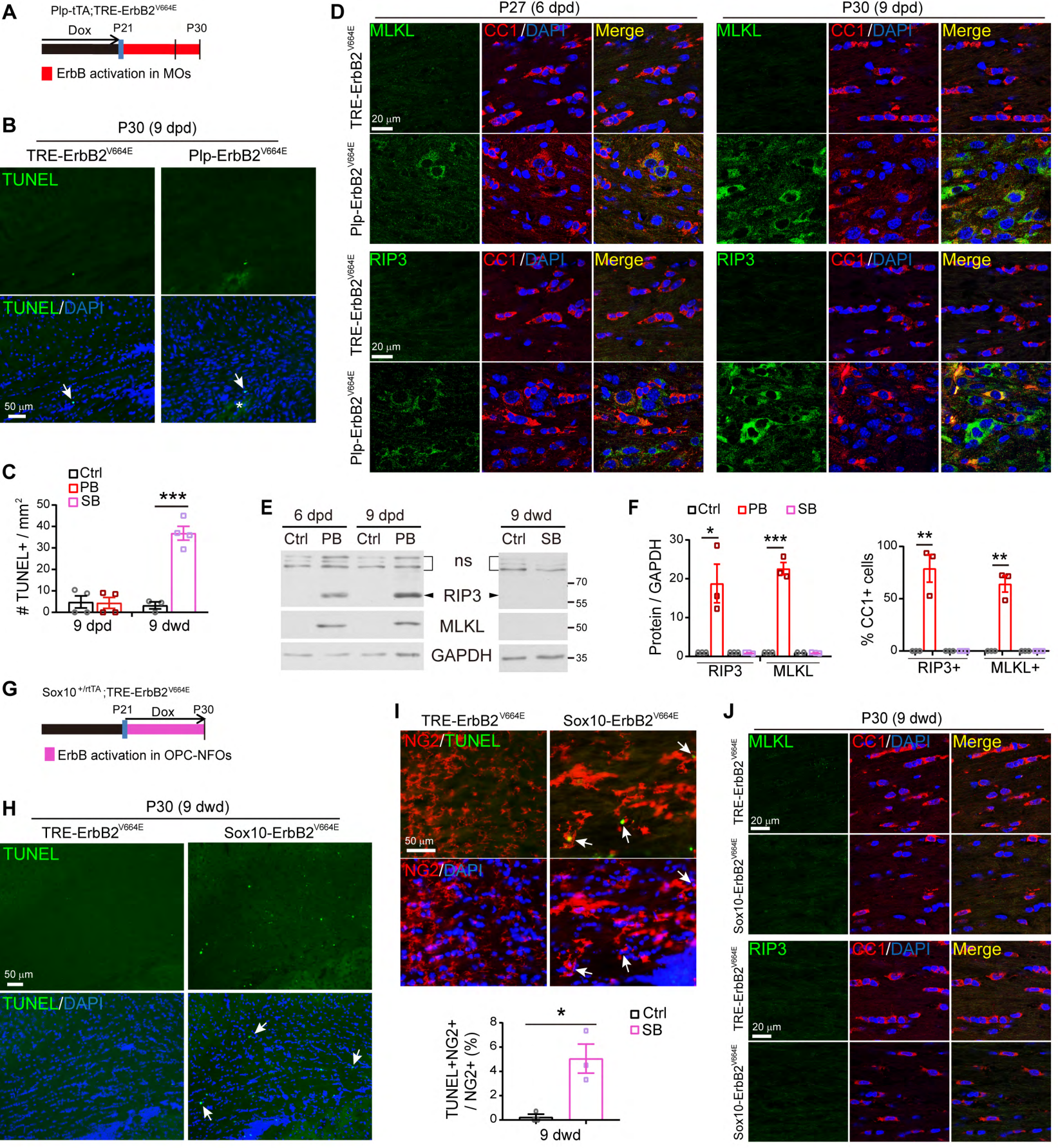
A
Plp-tTA;TRE-ErbB2V664E
Dox
P21
P30
ErbB activation in MOs
B
P30 (9 dpd)
TRE-ErbB2V664E
Plp-ErbB2V664E
TUNEL
TUNEL/DAPI
50 μm
C
Ctrl
PB
SB
TUNEL+ / mm2
9 dpd
9 dwd
D
P27 (6 dpd)
P30 (9 dpd)
MLKL
CC1/DAPI
Merge
RIP3
20 μm
E
6 dpd
9 dpd
9 dwd
Ctrl
PB
SB
ns
RIP3
MLKL
GAPDH
70
55
50
35
F
Protein / GAPDH
% CC1+ cells
RIP3
MLKL
RIP3+
MLKL+
G
Sox10+/rtTA;TRE-ErbB2V664E
ErbB activation in OPC-NFOs
H
P30 (9 dwd)
TRE-ErbB2V664E
Sox10-ErbB2V664E
I
NG2/TUNEL
NG2/DAPI
TUNEL+NG2+ / NG2+ (%)
J

Figure 6